

Bayesian inference of jet bulk-flow speeds in FRII radio sources

L. M. Mullin^{1*} and M. J. Hardcastle^{2†}

¹*Astrophysics Group, Cavendish Laboratory, University of Cambridge, J J Thomson Avenue, Cambridge CB3 0HE*

²*School of Physics, Astronomy and Mathematics, University of Hertfordshire, College Lane, Hatfield AL10 9AB*

Draft of 8 November 2018

ABSTRACT

Radio jet and core data for a complete sample of 98 FRII sources with $z < 1$ are analysed with a Markov-Chain Monte Carlo (MCMC) model fitting method to obtain constraints on bulk-flow speeds in the beam. The Bayesian parameter-inference method is described and demonstrated to be capable of providing meaningful constraints on the Lorentz factor at both kiloparsec and parsec scales. For both jets and cores we show that models in which some intrinsic dispersion is present in the features' intrinsic prominence, bulk-flow speeds or both provide the best fit to the data. The constraints on the Lorentz factor on parsec scales are found to be consistent with the expected values given VLBI observations and other evidence, with $\bar{\gamma} \approx 10$ –14. On kiloparsec scales, the Lorentz factor is found to be ≈ 1.18 –1.49, in agreement with the results of previous analyses of radio jet data. These values are clearly not consistent with the $\gamma \approx 10$ speeds required by beamed inverse-Compton models of X-ray emission from quasar jets; our results therefore support models that require velocity structure in powerful jets.

Key words: galaxies: active - galaxies: jets - radio continuum: galaxies.

1 INTRODUCTION

1.1 Relativistic beaming of jet emission

Fanaroff & Riley (1974) type II quasars and radio galaxies (hereafter FRIIs) generally exhibit double radio lobes with scales of tens to hundreds of kiloparsecs that are symmetrical about the source's central engine. There is now a very large amount of evidence for models (e.g. Scheuer 1974; Blandford & Rees 1974) in which these are supplied with energy, mass, momentum and magnetic flux by a bipolar, symmetrical, continuous flow of material – the ‘beam’ or ‘beams’. These outflows must persist and be well-collimated out to the 100-kpc scales of the lobes in order to give rise to the observed compact terminal hotspots. However, the observational signatures of these collimated outflows, ‘jets’ (e.g. Bridle & Perley 1984), are not always detected in FRIIs, either in the radio or at other wavebands. Where jet emission is observed, the jet is very often ‘one-sided’: i.e., it is either detected on one side of the source only or is very much brighter on one side. This is particularly characteristic of powerful FRII quasars. As the presence of twin beams is suggested by the morphology of the large scale structure, the fact that the detection of both jets in these powerful sources is so uncommon supports the hypothesis that the beam's emitting material is moving at relativistic speeds on kpc scales and that the emission is affected by Doppler boosting (‘beamed’). For the case of a source where the beam axis makes a relatively small angle to

the line of sight, as would be the case in standard unified models (Barthel 1989) for an FRII quasar, emission associated with the approaching jet is then Doppler-boosted and observable, while that associated with the receding jet is Doppler-suppressed and not detected. For a source where the beam axis lies close to the plane of the sky, both jets are likely to be Doppler-suppressed.

The key piece of evidence for relativistic beaming on kpc scales comes from the tendency for the jet side to be associated with the less depolarised lobe of the source, the Laing-Garrington effect (Garrington et al. 1988, Laing 1988). The depolarizing mechanism is believed to be an external Faraday screen in which the source is embedded, presumably the hot phase of the intergalactic medium, and thus the degree of depolarization observed depends upon the path length of the radiation through the screen. The less depolarized lobe is therefore expected to be the nearer lobe, or the lobe pointing towards us, and any correlation with the kiloparsec jet requires that the jet emission is Doppler-boosted. However, while observations of the Laing-Garrington effect require relativistic jet speeds on kiloparsec scales, they do not tell us what these speeds are.

Direct evidence for relativistic flow speeds in the *inner* regions of the beams, on parsec and sub-parsec scales, comes from VLBI observations of apparent superluminal motion. For example, Hough et al. (2002) have mapped the parsec scale regions of a complete sample of 25 lobe-dominated quasars (defined as having a ratio of nuclear to extended flux density at 5 GHz of less than 1) from the sample of Laing, Riley & Longair (1983, hereafter LRL). Of these sources, all have resolved structure on parsec scales, with one-sided jets detected on the same side as that of the kiloparsec jet where

* E-mail: lmm37@hotmail.co.uk

† E-mail: m.j.hardcastle@herts.ac.uk. Address postal correspondence to MJH.

such a jet is detected. Hough et al. estimate bulk flow speeds with Lorentz factor, γ , $\approx 5 - 10$ from multi-epoch observations, and these results are consistent with those from other observing programmes. Further observational support for the idea of high bulk speeds in radio-loud AGN in general comes from the rapid variability and consequent high brightness temperatures of parsec-scale features, the absence of very strong inverse-Compton emission in X-ray observations of the nucleus, and transparency to high-energy γ rays, which together imply bulk Lorentz factors $\gamma \geq 2$ and possibly as high as ~ 50 (Begelman, Fabian & Rees 2008). Arguments based on unification and population statistics (mostly in low-power objects; e.g. Chiaberge et al. 2000, Hardcastle et al. 2003) imply $\gamma \sim 3$: a plausible explanation for the widely differing γ values is that there is velocity structure in the parsec-scale jet. However, the essential point for our purposes is that all parsec-scale estimates agree on the need for Lorentz factors corresponding to speeds greater than $\sim 0.9c$, and the direct VLBI estimates imply speeds $\gtrsim 0.99c$ in general. It is therefore important to ask whether these speeds persist to the kiloparsec scale.

Two approaches to determining the kiloparsec-scale jet speed have been taken in the literature. The first uses the radio properties of the jets. This approach was pioneered by Wardle & Aaron (1997, hereafter WA97), who analysed the observed jet flux asymmetry in the 13 quasars imaged by Bridle et al. (1994). The jet flux asymmetry was defined as the observed jet flux over the counter-jet flux (where the counter-jet is the fainter of the two), but as for most sources no counter-jet was actually detected, many of their data points are actually lower limits. Taking into account the possibility of some intrinsic asymmetry, they simulated a number of data sets that were compared to the observed data by means of a Kolmogorov-Smirnov (K-S) test. They found that the observed data are best fitted with $0.6 \leq \beta \leq 0.8$, where β is the jet speed as a fraction of the speed of light. However, because their parent sample was not complete, they were forced to take quite a complex approach to the inclusion of the selection criteria in their analysis, and effectively to treat the upper limit on angle to the line of sight made by the beam axes of their sources as a free parameter in their fits. Hardcastle et al. (1999, hereafter H99), used a similar method to constrain the jet bulk-flow velocities for their sample of FRIIs with $z \leq 0.3$, which overlaps considerably with the sample considered in the present paper (see Section 2.1). Rather than using jet sidednesses they used the jet and core prominences (defined as the ratio between the jet/core flux density and that of the extended emission: see Section 2.4). Because their sample was complete the source orientation could be assumed to be random, simplifying the analysis with respect to WA97's work. In their analysis the free parameters were the intrinsic prominence, p_{int} , and β and, exploring a grid in these two parameters and using K-S tests in the same way, they derived speeds between $0.5c \sim 0.7c$. Arshakian & Longair (2004) used an analytic approach to the H99 data to infer slightly lower speeds, $\beta \approx 0.4$, on the basis of the jet sidedness distribution, while constraining $\beta > 0.6$ for the sample used by WA97. Thus all the approaches based on the distribution of the observed properties of the radio jets to date have been consistent in implying only moderately relativistic bulk speeds, $\beta \approx 0.5 \pm 0.1$.

However, a different approach is motivated by the widespread detection of strong X-ray emission from the jets of core-dominated quasars, believed to be the highly aligned counterparts of the FRII radio galaxies and lobe-dominated quasars studied by WA97 and H99. Following the discovery of the prototype of this class, PKS 0637–752 (Schwartz et al. 2000), it was quickly realised that the broad-band spectra of these object preclude a one-zone synchrotron

model for the radio through X-ray data, while various inverse-Compton models for the X-rays require extreme departures from equipartition for a non- or mildly relativistic jet. Instead, the model proposed independently by Tavecchio et al. (2000) and Celotti, Ghisellini, & Chiaberge (2001) is widely adopted. In this model, the jet is moving relativistically, with a bulk Lorentz factor $\gamma \gg 1$. As seen by the jet, the energy density in the microwave background increases by a factor of the order γ^2 , and this increases the emissivity of the inverse-Compton scattering of the microwave background (hereafter CMB/IC) in the jet frame; in PKS 0637–752, crucially, the γ (~ 10) required for the kpc-scale jet is very similar to that inferred from VLBI studies of superluminal motion in the nucleus. The emission from this process is strongly anisotropic and so is only visible in core-dominated objects, but, in unified models, the jets in lobe-dominated quasars and FRII radio galaxies must have comparable speeds. The implication of $\gamma \gg 1$ in the kpc-scale jets of all radio-loud objects is in strong contrast to the results of the prominence/sidedness analyses described above.

How can these two very different estimates of the kpc-scale jet speed be reconciled? There is still disagreement in the literature over whether the beamed CMB/IC model really does describe all, or even any, of the observed quasar jets (e.g. Stawarz et al. 2004, Hardcastle 2006, Jester et al. 2007). If it does, then, as argued by Hardcastle (2006), velocity structure in the kiloparsec-scale jets and perhaps bulk deceleration on hundred-kpc scales seem inevitable consequences. At the same time, though, the existing work on the radio data is open to a number of criticisms. The K-S test is not really adapted to model fitting (that is, it is not obvious that maximizing the K-S test null hypothesis probability really corresponds to maximizing the likelihood). More seriously, the large number of jet or counterjet non-detections and consequent limits on sidedness or prominence measurements are hard to take into account either in the K-S method of WA97 or H99 or in the analytical method of Arshakian & Longair (2004), although H99 attempted to assess the effect of the limits in their sample by scaling them and argued that they did not have a strong effect. In all cases the sample sizes are small; additionally, WA97's sample has complex selection effects while H99's sample is low-luminosity and contaminated by low-excitation radio galaxies whose role in unified models is not clear. For all these reasons, it is worth revisiting the radio-based estimates of kpc-scale jet speeds with new data and new analysis techniques: the present paper presents the results of such a study.

1.2 This paper

The present paper is based on the work of Mullin, Riley & Hardcastle (2008, hereafter Paper I). In that paper we presented a detailed study of the observed properties of a complete sample of FRII sources, including the kiloparsec-scale jets and core features. We concluded that the observational evidence supports the beaming hypothesis and that, while there is stronger evidence for relativistic speeds on parsec scales, the observed correlation between jet and core brightness implies the extension of high bulk-flow speeds into kiloparsec scales.

In this paper we use these jet and core data together with a Bayesian inference method in order to constrain Lorentz factors in the beams on parsec and kpc scales. Our approach is free from many of the disadvantages of earlier work. We do not carry out systematic grid searches of parameter space, and so are not limited to a small number of model parameters: this allows us to deal with the case in which the intrinsic prominence and speed distributions are not delta functions but themselves have some intrinsic scatter.

Crucially, we can also treat the limits in the data properly, rather than treating them as measurements. In addition, our dataset is a factor ~ 2 larger than that of H99, and contains luminous quasars and powerful radio galaxies which are well matched to the core-dominated quasars for which high bulk Lorentz factors have been inferred. This paper therefore represents a significant improvement over previous work.

The remainder of the paper is structured as follows. In the following Section the dataset is described, while the analysis method and performance of the code used is discussed in Section 3. Results are presented in Section 4 and the discussion and conclusions are in Section 5.

Throughout the paper we use the quantities measured and calculated in Paper I: this implies the use of a cosmology with $H_0 = 70 \text{ km s}^{-1} \text{ Mpc}^{-1}$, $\Omega_m = 0.3$ and $\Omega_\Lambda = 0.7$. All symbols used are summarized in Table 1.

2 THE DATA

2.1 The sample

The sample is that of Paper I, which consists of the 98 FR II radio galaxies and quasars with $z < 1$ in the sample of LRL. This is a complete flux-limited sample, including all 3CR sources observed to have $S_{178} > 10.9 \text{ Jy}$ (on the scale of Baars et al., 1977) with declination $> 10^\circ$ and $|b| > 10^\circ$, where S_{178} is the total source flux measured at 178 MHz. At this low frequency the source flux is dominated by the diffuse emission of the large scale lobe structure and as such little contribution should be made by Doppler-boosted components; thus the selection criterion should ensure that the sample is not biased with respect to orientation.

A long-term observing project has mapped the vast majority of these 98 sources at high resolution and sensitivity with the VLA telescope. Data from this project have been presented in a series of papers: Black et al. (1992), Leahy et al. (1997), Hardcastle et al. (1997), Gilbert et al. (2004) and, most recently, Mullin, Hardcastle & Riley (2006). Observations of the outstanding sources have been made by us or by other workers and the data are available in the literature; all references to the data used here are given in Paper I. In addition, the data – maps and measurements – from Paper I are now available on-line¹. The subsample of sources with $z \leq 0.3$ overlaps considerably with that of H99, and the measurements of H99 are used for the sources that we have in common, but the larger redshift range of our sample gives us a factor 2 more sources (improving the statistical significance of our results) and means that 15 FR II quasars are included, complementing the data on broad- and narrow-line radio galaxies from H99’s work.

2.2 Jets

The definition of the term jet and a discussion of the data and measurements is given in Paper I. Here, the jet criteria are reiterated: they are based on those of Bridle & Perley (1984). Thus, a jet is any feature that is

- (i) at least four times as long as it is wide;
- (ii) separable at high resolution from other extended structures (if any), either by brightness contrast or spatially (e.g. it should be

a narrow ridge running through more diffuse emission, or a narrow feature in the inner part of the source entering more extended emission in the outer part).

In some sources jets appear to bend, and this causes problems for analysis in terms of beaming models, which must assume a single angle to the line of sight θ , as discussed by Bridle et al. (1994). We follow Bridle et al. (1994) and H99 in defining the straight jet, which satisfies the above two criteria but also must be aligned with the compact radio core where it is closest to it (and is measured from the end closest the core along its length only while the deviation from a straight line is less than the jet radius). Only the flux density of the straight jet is used in the analysis in this paper.

In practice, the straight jet is taken to be the longest straight section of the jet in the source that is aligned with the core. Using the AIPS task TVSTAT, the integrated flux within the region containing the apparent jet emission, F_{obs} , was found. Background flux was corrected for by taking measurements of two regions identical in size to the initial jet measurement to the immediate right and left of the feature. The average of these, B_{obs} , was then subtracted from the jet measurement to give the observed jet flux, $J_{\text{obs}} = F_{\text{obs}} - B_{\text{obs}}$. In order to get the best estimate of J_{obs} , three values of jet flux were taken this way and averaged. The greatest source of error in the jet measurement is considered to arise from the ambiguity in defining the jet emission itself: the errors quoted are therefore based on the range of the three jet measurements made. Where no jet emission is detected, an upper limit is estimated by measuring the integrated flux of a region ≈ 2 restoring beam widths across the entire distance between the core and primary hotspot region. Background flux is corrected for in the same manner as for the detected jets by taking two further integrated flux measurements either side of the initial region. However, if the flux associated with the central region is not the highest of the three, then the upper limit estimate is taken to be the positive difference between the central measure and the lower of the other two.

The sample extends over a large range in redshift and was observed using a variety of different telescopes and telescope configurations, which means that the effective (spatial) observing resolution is far from constant across the sample. Observational effects on jet detectability were considered in Paper I, where we concluded that, although observing resolution is clearly a factor in jet visibility, there is no simple *systematic* bias across the sample nor any trend with redshift. We therefore do not expect that the variations in effective observing resolution will affect the robustness of the results of any analysis of $p_{\text{obs},j}$.

2.3 Cores

Paper I also contains a detailed discussion of core measurements. The core measurements were obtained from the highest-resolution map available for a given source using the AIPS task JMFIT, which fits an elliptical Gaussian model of between one and four components to a feature. One component was fitted and the peak intensity found was taken as the core flux. As most cores in the sample were unresolved at all resolutions such a model fitted the data well. Errors were determined from the square root of the average of the squared formal errors returned from the fitting procedure. For around two thirds of the sample this error is less than 2 per cent of the core flux, so the calibration error (expected to be 2-3 per cent) will dominate. Errors quoted therefore correspond to 3 per cent of the core flux measurement, unless the formal error from JMFIT is greater, in which case the latter is quoted. Cores were undetected

¹ See <http://zll.extragalactic.info/>

in only seven sources, and in these cases estimates of upper limits were made from the off-source noise.

Again, observing effects were considered for the core prominence data in Paper I. We concluded that, as the cores are typically bright, unresolved features that are generally much brighter than any lobe or jet material with which they might be confused at low resolution, observational effects are not a source of systematic bias in the analysis of $p_{\text{obs,c}}$.

2.4 Prominence

In order to analyse the jet and core data the observed jet and core flux density data are extrapolated to a common frequency of 8.4 GHz and then K-corrected assuming the spectral index, α , = 0.5 for jets and = 0 for cores, before being converted to a luminosity using the relation

$$P = R^2(1+z)^2 S \quad (1)$$

where P is the jet or core luminosity, R the proper distance (as calculated using the ANGSIZ² code) and S the jet or core flux density. The total source flux measured at 178 MHz is K-corrected using the low-frequency spectral index, α_{lf} (appropriate over the range 178 – 750 MHz), and converted to a luminosity, P_{178} . The jet and core prominence are then the ratio of the corresponding feature's luminosity to P_{178} . Observed jet and core prominences for our sample are plotted in Figs 1 and 2.

This definition of prominence, which we used in Paper I, assumes that the total source flux as measured at 178 MHz is uncontaminated by beamed components. It is expected that the sample will be dominated by the extended lobe emission at this low frequency; however, in sources with very bright jet or core features it is not clear that no contamination exists and this is potentially a source of bias in the prominence values. We investigated whether there is any evidence for such contamination in our data by comparing prominence values evaluated as described above with those evaluated with a modified total source flux, that is, a total source flux corrected by subtracting off jet and core features.

The modified total source flux at 178 MHz was calculated by extrapolating the jet and core fluxes from the observed frequency to 178 MHz. Here, the *total* jet was used, that is, the feature that satisfies the jet conditions as specified in Section 2.2 and not the more restrictive *straight* jet conditions (see Paper I for a more detailed description of total and straight jet definitions). Both jet and counter-jet features were extrapolated back to 178 MHz. The corrected fluxes were then subtracted from the total source flux, and this modified total source flux was K-corrected and used to evaluate the core and straight jet prominence as described above.

Plotting these alternative jet and core prominence values against those initially determined, there was no evidence that either the core or jet prominence values were greatly affected by contamination of beamed components if the total source flux at 178 MHz is used without first correcting it – the correlation in the plots is linear and there is no trend for sources to curve away from this line. Additionally, considering the errors in the jet and core flux measurements, the difference in prominence values made by modification of the total source flux is low – in particular, the difference in the jet prominence made by modifying the total source flux is typically a fraction of a percent of the quoted error.

From this we conclude that using the 178 MHz total source

flux without making any attempt to remove beamed emission to define prominence, as we did in paper I, will not affect the robustness of our analysis. We therefore use the unmodified prominence for consistency with Paper I.

Finally, we note that in Paper I a spectral index of 0.5 was used for jets, despite the fact that higher values of ≈ 0.8 have typically been used by other workers (H99, for example). Hotspot features are expected to be associated with much flatter spectra than jets and it was decided in the previous analysis, given that trends in core, jet and hotspot properties as well as correlations between the features were being considered, that a spectral index of 0.5 should be used for both jet and hotspot features. The analysis presented here uses the jet prominence data of Paper I; however, we consider the effects of varying α for jets in Section 4.1.

3 DATA MODELS

3.1 Doppler boosting of source emission

The emission from any component of a radio source that is travelling at a significant fraction of the speed of light with respect to an Earth-bound observer will be anisotropic due to relativistic beaming even if it is isotropic in the rest frame (in this paper we neglect the minor effects due to intrinsic anisotropy of emission in jets: see H99 for more discussion). As received on Earth, a feature will have an observed flux density, $S_{\nu_{\text{obs}}}$, given by

$$S_{\nu_{\text{obs}}} = S_{\nu_{\text{rest}}} (\gamma[1 - \beta \cos \theta])^{-m+\alpha} \quad (2)$$

(e.g. Ryle & Longair 1967; Bridle et al. 1994) where $S_{\nu_{\text{rest}}}$ is the flux density of the feature in the emitter's rest frame, β is the fraction of the speed of light at which the emitter is traveling, γ is the Lorentz factor ($= 1/\sqrt{1-\beta^2}$), θ is the angle of the velocity vector to the line-of-sight, α is the spectral index of the radiation (where $S \propto \nu^{-\alpha}$) and m is a constant reflecting the geometry of the beamed component. Following Scheuer & Readhead (1979) and Lind & Blandford (1985), the value of m taken here to be appropriate for a continuous jet is 2. As the spectral index appears in the exponent of the Doppler factor, it follows that, all other things being equal, a larger assumed α gives rise to a stronger beaming effect.

3.2 Jets

Applying equation (2) to the jet features in the sample, we obtain the relationship between the observed jet prominence, $p_{\text{obs,j}}$, and the intrinsic jet prominence, $p_{\text{int,j}}$:

$$p_{\text{obs,j}} = p_{\text{int,j}} [\gamma(1 - \beta \cos \theta)]^{-2+\alpha} \quad (3)$$

where α is the adopted spectral index of the jet, $p_{\text{int,j}}$ is the intrinsic, rest-frame prominence of the jet feature and θ is the orientation of the jet with respect to the observer's line of sight (γ, β are as before). Here we assume that the normalizing luminosity (P_{178} in our case) is unaffected by beaming, as discussed above.

3.3 Cores

The core emission is thought to originate in the inner parsecs of the beam, that is, the parsec-scale bipolar jets, and so the model of

² <http://ascl.net/angsiz.html>

equation (2) can be applied to the observed core prominence in the following manner, assuming that for cores $\alpha = 0$:

$$p_{\text{obs}_c} = p_{\text{int}_a} [\gamma_a (1 - \beta_a \cos \theta_a)]^{-2} + p_{\text{int}_r} [\gamma_r (1 - \beta_r \cos \theta_r)]^{-2} \quad (4)$$

where the subscripts ‘a’ and ‘r’ correspond to the approaching and receding parsec scale jet respectively. Again the subscript ‘int’ indicates the intrinsic, rest frame prominence of these jets and θ , γ and β are as before. In the simplest models, which we adopt throughout the paper, $p_{\text{int}_a} = p_{\text{int}_r} = 0.5 \times p_{\text{int}_c}$, $\theta_r = 180^\circ - \theta_a = 180 - \theta$ where θ has the same value as for the kpc-scale jet, $\beta_r = \beta_a = \beta_c$ and $\gamma_r = \gamma_a = \gamma_c$.

3.4 Model Fitting Method

3.4.1 Beaming Model Validity

As discussed in Section 1.1, previous workers have used jet and core models of the form given in equations (3) and (4) to constrain γ values. An advantage of the present analysis method over these studies is the possibility to allow for distributions in the intrinsic prominence and γ parameters. Arguments have been made (e.g. Urry & Shafer 1984) that the intrinsic jet or core prominence might be expected to be a fixed fraction of the intrinsic total source flux, but, while this is a useful simplifying assumption, it is more likely that there will be a range in intrinsic prominence values in the sample, since if nothing else there will be scatter in the relationship between the total (normalizing) luminosity and the intrinsic jet power.

In the present paper the nature of such distributions is assumed to be normal or log-normal in the case of jets, since such distributions are appropriate to cases in which the observed values are the sum, or product, of many variable factors. This is also the case for the cores, but in this case we also consider a model based on power-law distributions. There have been a number of studies in the literature of samples of VLBI observations in terms of the apparent velocities and luminosities, often including model fitting to obtain information on the probable γ s and luminosity functions. In these studies, a power-law distribution for γ is often assumed. For example, Urry & Padovani (1990) consider the effects of allowing such a distribution in the bulk Lorentz factors in their analysis, arguing that it allows both low or high values of γ to be favoured, but also that a wide Gaussian distribution would resemble a flat power-law. Subsequent studies, such as Lister & Marscher (1997), and more recently Cohen et al. (2007), find that model fitting based on such distributions is consistent with the data, though no evidence that such a model is to be *favoured* is reported. Given this other work, applying a power-law distribution to the core data provides an interesting comparison to models based on a normal distribution. A uniform distribution in $\cos \theta$ is used for θ , assuming that the sample sources are randomly aligned with respect to the observer’s line of sight.

Examples of simulated data sets using this approach and the beaming models of equations (3) and (4) are plotted together with the observed data in Figs 1 and 2. It can be seen that the shape of the resulting distributions can give a good representation of the true observed distributions. (Note that the simulated data sets shown are not fitted to the data in any way other than by simple scaling, though the parameters used are representative of those we obtain in subsequent sections by fitting.) The observed jet and core prominence is strongly determined by γ in each case. The effect of beaming on the shape of the observed prominence with respect to the normally distributed intrinsic prominence is to suppress the observed emis-

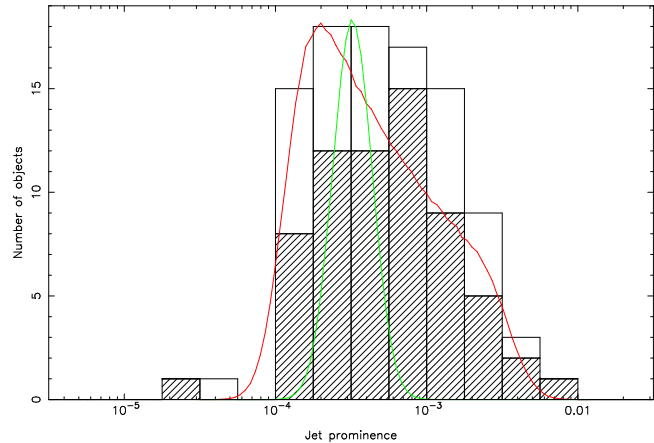


Figure 1. Histogram of the observed jet prominence data, p_{obs_j} . Filled regions indicate measurements and empty regions upper limits. The data are compared (solid lines) with the expected distribution jet prominence from a simulation with $\gamma = 1.5$ (broad curve, red) and the corresponding distribution of intrinsic prominence (narrower curve, green), renormalized to a common maximum value for convenience of presentation. p_{int_j} has a log-normal distribution with $\sigma = 0.3$ (in units of the natural logarithm) around $\ln(p_{\text{int}_j}) = -8$.

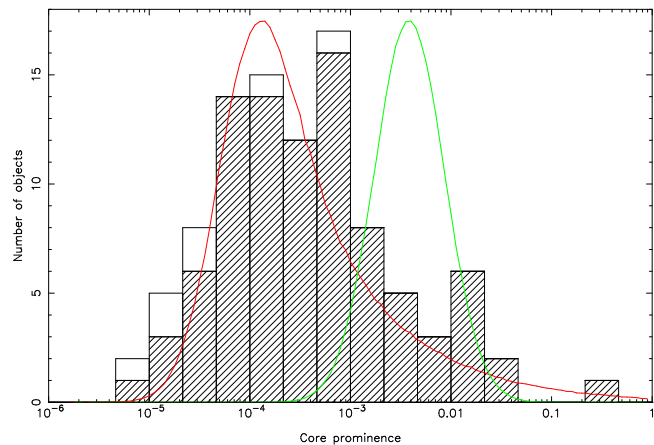


Figure 2. Histogram of the observed core prominence data, p_{obs_c} . Regions and curves are as in Fig. 1. Here the simulated data have $\gamma = 10.0$ and p_{int_c} has a lognormal distribution with $\sigma = 0.8$ (in units of the natural logarithm) around $\ln(p_{\text{int}_j}) = -5.5$.

sion in many sources, while boosting it in a smaller fraction. As γ increases this effect is more pronounced. Changes in the mean of the intrinsic prominence distribution affect the observed prominence distribution’s location on the x -axis but not its shape: it acts as a scale factor. Changes in the intrinsic scatter that we assume broaden the distribution (and are thus to some extent degenerate with changes in γ) but also tend to smooth out the resulting distribution.

Therefore, while the problem is degenerate, with at least three unknown parameters (intrinsic prominence, orientation and γ), it is clear that analysis of the observed prominence distribution can tell us something about beaming in the sample.

Table 1. Glossary for symbols used.

Symbol	Parameter	Definition
β	speed as a fraction of the speed of light	Section 1.1
p_{int}	intrinsic prominence of the jet or core feature	Section 1.1
S_{178}	total source flux measured at 178 MHz	Section 2.1
F_{obs}	measured jet flux	Section 2.2
B_{obs}	jet background flux correction	Section 2.2
J_{obs}	background-corrected jet flux	Section 2.2
α	spectral index	Section 2.4
P	jet or core observed luminosity	Section 2.4
R	proper distance	Section 2.4
S	jet or core flux density	Section 2.4
α_{lf}	low frequency spectral index	Section 2.4
P_{178}	source luminosity, as measured at 178 MHz	Section 2.4
$S\nu_{\text{obs}}$	observed flux density	Section 3.1
$S\nu_{\text{rest}}$	flux density in emitter's rest frame	Section 3.1
γ	bulk Lorentz factor	Section 3.1
m	constant reflecting the geometry of the beamed component	Section 3.1
p_{obs_j}	observed jet prominence	Section 3.2
p_{int_j}	intrinsic jet prominence	Section 3.2
θ	angle of emitter's trajectory with respect to observer's line of sight	Section 3.2
p_{obs_c}	observed core prominence	Section 3.3
p_{int_c}	intrinsic core prominence	Section 3.3
p_{int_a}	intrinsic prominence of approaching parsec scale jet	Section 3.3
p_{int_r}	intrinsic prominence of receding parsec scale jet	Section 3.3
γ_a	bulk Lorentz factor of approaching parsec scale jet	Section 3.3
γ_r	bulk Lorentz factor of receding parsec scale jet	Section 3.3
β_a	approaching parsec scale jet speed as fraction of speed of light	Section 3.3
β_r	receding parsec scale jet speed as fraction of speed of light	Section 3.3
θ_a	angle of approaching emitter's trajectory with respect to observer's line of sight	Section 3.3
θ_r	angle of receding emitter's trajectory with respect to observer's line of sight	Section 3.3
H	hypothesis	Section 3.4.2
D	observed data	Section 3.4.2
I	prior information about D	Section 3.4.2
$P(H D, I)$	posterior probability of H given D and I	Section 3.4.2
$P(H I)$	prior probability of H	Section 3.4.2
$P(D H, I)$	likelihood of D given H and I	Section 3.4.2
$P(D I)$	evidence	Section 3.4.2
p_{mod}	expected observed prominence corresponding to model parameter values	Section 3.4.2
$P(p_{\text{mod}_{t+1}} p_{\text{mod}_t})$	transition probability	Section 3.4.2
p_{can}	candidate value for next chain step	Section 3.4.2
$Q(p_{\text{can}} p_{\text{mod}_t})$	proposal distribution	Section 3.4.2
$\alpha(p_{\text{mod}_t}, p_{\text{can}})$	acceptance probability	Section 3.4.2
r	metropolis ratio	Section 3.4.2
λ	factor by which the posterior is scaled in burn-in	Section 3.4.2
$\bar{\gamma}$	mean bulk Lorentz factor	Section 3.4.4
γ_{min}	upper limit on γ	Section 3.4.4
γ_{max}	upper limit on γ	Section 3.4.4
\bar{p}_{int}	mean intrinsic prominence	Section 3.4.4
σ_γ	intrinsic dispersion in $\gamma/\bar{\gamma}$	Section 3.4.4
$\sigma_{p_{\text{int}}}$	intrinsic dispersion in prominence	Section 3.4.4
a	power-law index for power-law Lorentz factor distribution	Section 3.4.4
X	general symbol for parameters	Section 3.4.6
M	model	Section 3.4.6
O_{ik}	Bayes factor	Section 3.4.6
$\bar{\gamma}_j$	mean bulk Lorentz factor for the jets	Section 4.2
$\bar{\gamma}_c$	mean bulk Lorentz factor for the cores	Section 4.3

3.4.2 MCMC approach

The discussion in the following sections is only a very brief introduction to the MCMC approach to Bayesian inference; more detailed treatments can be found in the literature [e.g., Gregory (2005) and references therein].

We can obtain the posterior probability of a hypothesis H from Bayes' theorem:

$$P(H|D, I) = P(H|I) \frac{P(D|H, I)}{P(D|I)} \quad (5)$$

where D is the observed data and I is the prior information we have about D , $P(H|I)$ is the prior probability of H , $P(D|H, I)$ is its likelihood and $P(D|I)$ is the normalization factor, the 'evidence'. In the present problem, we have observed prominence data, p_{obs} . If we define a parameter space in terms of p_{int} , γ and θ , we can evaluate the expected observed prominence, p_{mod_i} , corresponding to a parameter set drawn from this space using equation (3) or (4) as appropriate. We can then determine the posterior probability of p_{mod_i} , $P(p_{\text{mod}_i}|p_{\text{obs}}, I)$, by evaluating $P(p_{\text{mod}_i}|I)$, $P(p_{\text{obs}}|p_{\text{mod}_i}, I)$ and $P(p_{\text{obs}}|I)$.

The obvious problem is that, with a minimum of three parameters, the exhaustive computation of the probability distribution corresponding to the defined parameter space is not feasible. Straightforward Monte Carlo could provide a good approximation – the method is to draw uniform, randomly distributed, independent samples from the distribution and its accuracy is determined by the number of these samples. However, this approach is still computationally expensive and much time can be spent in regions where the probability is very small. Instead, MCMC is more efficient as it exploits the fact that samples need *not* be drawn independently if they are generated from the target distribution or some function of it, here $P(p_{\text{mod}}|p_{\text{obs}}, I)$, in the correct proportions.

The Metropolis-Hastings algorithm is used to apply the method. This algorithm generates a sample set by constructing a walk through parameter space in which the probability of a sample's being in some region of space is proportional to the posterior density for that region. It does this by determining the next chain step, which in this case is $p_{\text{mod}_{t+1}}$, with respect to its probability given the current chain step, p_{mod_t} , through the evaluation of the transition probability (or kernel), $P(p_{\text{mod}_{t+1}}|p_{\text{mod}_t})$.

The algorithm chooses a candidate value for $p_{\text{mod}_{t+1}}$, p_{can} , from a proposal distribution, $Q(p_{\text{can}}|p_{\text{mod}_t})$ that is understood and easy to evaluate (see Section 3.4.3). p_{can} is accepted or rejected as $p_{\text{mod}_{t+1}}$ as determined by the acceptance probability, $\alpha(p_{\text{mod}_t}, p_{\text{can}})$ which can be expressed as

$$\begin{aligned} \alpha(p_{\text{mod}_t}, p_{\text{can}}) &= \min(1, r) \\ &= \min\left(1, \frac{P(p_{\text{can}}|D, I) Q(p_{\text{mod}_t}|p_{\text{can}})}{P(p_{\text{mod}_t}|D, I) Q(p_{\text{can}}|p_{\text{mod}_t})}\right) \end{aligned} \quad (6)$$

where r is the Metropolis ratio. If $r \geq 1$, then p_{can} is accepted and $p_{\text{mod}_{t+1}} = p_{\text{can}}$. If $r < 1$, then a random variable U is sampled from a uniform distribution in the interval 0 to 1. In the case that $U \leq r$, $p_{\text{mod}_{t+1}} = p_{\text{can}}$, otherwise p_{can} is rejected. The transition kernel, the probability that the algorithm will draw and accept a sample $p_{\text{mod}_{t+1}}$ given the chain's present state, is then

$$P(p_{\text{mod}_{t+1}}|p_{\text{mod}_t}) = Q(p_{\text{mod}_{t+1}}|p_{\text{mod}_t})\alpha(p_{\text{mod}_t}, p_{\text{can}}) \quad (7)$$

As a first consideration, we might want the proposal distribution, $Q(p_{\text{can}}|p_{\text{mod}_t})$, to be the target distribution itself – but of course, this is unknown as it is this that we are trying to evaluate. However, if the Markov chain is irreducible, aperiodic and positive recurrent

then it can be shown that there exists a stationary distribution from which all samples will be drawn subsequently once one initial sample is drawn; thus the algorithm will converge on this stationary distribution for a wide range of proposal distributions.

The probability of drawing p_{mod_t} from the posterior is $P(p_{\text{mod}_t}|D, I)$ and the probability that $p_{\text{mod}_{t+1}}$ is subsequently drawn and accepted is given by the joint probability of p_{mod_t} and $p_{\text{mod}_{t+1}}$: $P(p_{\text{mod}_t}, p_{\text{mod}_{t+1}})$, which can be expressed as the following:

$$P(p_{\text{mod}_t}, p_{\text{mod}_{t+1}}) = P(p_{\text{mod}_t}|D, I)P(p_{\text{mod}_{t+1}}|p_{\text{mod}_t}) \quad (8)$$

Expanding this out using equations (6) and (7), gives the detailed balance equation:

$$P(p_{\text{mod}_t}|D, I)P(p_{\text{mod}_{t+1}}|p_{\text{mod}_t}) = P(p_{\text{mod}_{t+1}}|D, I)P(p_{\text{mod}_t}|p_{\text{mod}_{t+1}}) \quad (9)$$

From this it can be seen that the stationary distribution is the target distribution of the chain, irrespective of the proposal distribution – $Q(p_{\text{can}}|p_{\text{mod}_t})$ – initially used. The sampling process before the stationary distribution is reached is referred to as burn-in.

The algorithm allows the chain to move to regions of increasing probability while sometimes accepting a chain step of lower probability. This contributes to the efficient exploration of parameter space as the chain can move away from regions of local maxima. However, for a target posterior distribution of a multi-dimensional problem this flexibility will not necessarily be sufficient to prevent the chain becoming stuck in a local maximum region; the results will still be dependent on the starting sample. In practice we use multiple chains with information exchange (see the next section) but we also make use of a simulated annealing method that allows a modified posterior distribution to be sampled during burn-in.

This modified posterior distribution is defined as

$$p(p_{\text{obs}}|D, I) = p(p_{\text{obs}}|I)p(D|p_{\text{obs}}, I)^\lambda \quad (10)$$

where λ may take values between 0 and 1. When $\lambda = 0$ the samples are drawn just from the prior distribution, which will typically be much flatter than the likelihood function – if this is the case increasing λ draws samples from an increasingly peaked function until the posterior itself is being sampled when $\lambda = 1$. Sampling from the flatter distributions gives the sampler better opportunity to reach all regions of the posterior probability distribution, even in the presence of many local maxima. The general practice is to determine the rate at which λ is increased from 0 to 1 (the annealing schedule) such that it will correspond to the burn-in period. In this scheme, once $\lambda = 1$ sampling is being made from the target distribution. The rate at which λ should be increased is then subjective and determined by experiment.

3.4.3 Implementation

Our implementation of the Metropolis-Hastings algorithm is heavily based on the approach of Hobson & Baldwin (2004), as implemented in the METRO sampler code, kindly provided to us by Mike Hobson. We implemented the basic algorithm in modular C using the Message Passing Interface (MPI) framework to allow it to run on a cluster of multi-core computers; only the functions that implement the likelihood function and priors need be modified for a particular problem. At run-time the code separates into one master and one or more slave threads; in general it is advantageous to have as many slave threads as there are available CPUs.

Each slave carries out a separate and (except as discussed below) independent Metropolis-Hastings run with burn-in (a 'chain'),

starting in a random point in the prior parameter space. As discussed by Hobson & Baldwin, multi-threading of this kind greatly reduces the chances of getting stuck in a local minimum in parameter space; it also allows us to speed up by a factor of the number of available computing cores the sampling of the posterior probability distribution. We borrow from the METRO code the concept of ‘engines’, which are different versions of the proposal distribution Q . Several engines are available, and the code picks the one to use for each trial at random, using probabilities that we have assigned based on our experience with the code. The active engines in the implementation of the code used here are ‘take a random step in a single dimension of the problem’, ‘take a random jump in all dimensions of the problem simultaneously’, ‘jump to a random point in parameter space’ and ‘jump in one dimension to the current position of another thread’ (allowing cross-mixing). The sizes of the random steps used in the first two engines are adaptively chosen during burn-in to achieve a reasonable ratio of success to failure, but are fixed thereafter.

The master thread records the accepted samples of all the slave threads in a file, and also co-ordinates synchronization and communication between the slave threads. The final result when all slave threads are completed is a large file giving the co-ordinates in parameter space of all accepted samples both before and after burn-in. The density of points in a given (necessarily finite) region of n -dimensional parameter space is proportional to the posterior probability of the model parameters lying in that region. Estimated value determination, credible interval estimates, plotting and evidence determination can then all be carried out using this file. The burn-in points are discarded for most applications, but are used for evidence determination, as discussed below.

3.4.4 Model parameters and priors

Our basic model for jets and cores (hereafter ‘the basic model’) has up to 4 parameters.

(i) $\bar{\gamma}$, the mean bulk Lorentz factor. We adopt a uniform (uninformative) prior in the range $1.. \gamma_{\max}$ for this quantity. γ_{\max} throughout our fitting is taken to be 5.5 for jets and 20.0 for cores.

(ii) \bar{p}_{int} , the mean intrinsic prominence. As this is a scale parameter, we adopt a uniform prior in $\ln(\bar{p}_{\text{int}})$ between two values chosen to cover all reasonable values of parameter space. This avoids bias towards large values (Gregory 2005).

(iii) σ_{γ} , the intrinsic dispersion in the bulk Lorentz factor. Lorentz factors of simulated sources are drawn from a normal distribution with mean $\bar{\gamma}$ and standard deviation $\bar{\gamma}\sigma_{\gamma}$, truncated so that $\gamma \geq 1$ in all cases. The case $\sigma_{\gamma} = 0$ is equivalent to a delta function in Lorentz factor. We adopt a uniform prior for σ_{γ} between 0 and 0.6.

(iv) $\sigma_{p_{\text{int}}}$, the intrinsic dispersion in the prominence. Since the observed prominence will be the product of a number of independent variables, it is appropriate to draw simulated prominences from a lognormal distribution with mean $\ln(\bar{p}_{\text{int}})$ and standard deviation $\sigma_{p_{\text{int}}}$; the case $\sigma_{p_{\text{int}}} = 0$ is equivalent to a delta function in intrinsic prominence. We adopt a uniform prior for $\sigma_{p_{\text{int}}}$ between 0 and 6.

For cores, we also investigated a model (hereafter ‘the power-law model’, as discussed in Section 3.4.1) in which the Lorentz factor follows a power-law distribution between two limits, γ_{\min} and γ_{\max} , with a power-law index a , i.e. $P(\gamma) \propto \gamma^{-a}$. For these parameters we adopted uniform priors between 1 and 5 for γ_{\min} , between 10 and 40 for γ_{\max} , and between 0 and 5 for p . Since

the mean intrinsic prominence \bar{p}_{int} is a required component of this model, and a dispersion in the intrinsic prominence, parametrized as above by $\sigma_{p_{\text{int}}}$, may also be considered, the model has up to 5 parameters.

3.4.5 Likelihood calculation

The likelihood is the probability of obtaining a given set of intrinsic prominences, p_{obs} , given the model and the priors, i.e. $\prod_k P(p_{\text{obs}_k} | p_{\text{mod}}, I)$. In general it is difficult to write down the likelihood function for the type of models discussed in Section 3.4.4 analytically. We therefore proceed by Monte Carlo methods. For the set of model parameters determined by the Metropolis-Hastings algorithm, we simulate a set of N model prominences on the beaming equations (equations 3 and 4) and the dispersions discussed in Section 3.4.4 and with an appropriate distribution of the angle to the line of sight θ (in practice we assume sources randomly oriented to the line of sight in all models, so θ values are drawn from a uniform distribution in $\cos \theta$). By construction, these simulated prominences are distributed with the appropriate probability distribution for the model being tested. The probability of obtaining any given observed value of the prominence, p_{obs_k} , with an associated error, assumed Gaussian, of $\sigma_{p_{\text{obs}_k}}$ given the model is then given by

$$P(p_{\text{obs}_k} | p_{\text{mod}}, I) = \frac{1}{N} \sum_{i=1}^N \exp \left\{ -\frac{(p_{\text{obs}_k} - p_{\text{mod}_i})^2}{2\sigma_{p_{\text{obs}_k}}^2} \right\} \quad (11)$$

Essentially here we are Monte Carlo integrating over the product of the probability distribution for the data point and the probability distribution for the given model, with a suitable normalization. In the case where p_{obs} is an upper limit, we could simply write

$$P(p_{\text{obs}_k} | p_{\text{mod}}, I) = \frac{1}{N} \sum_{i=1}^N l(p_{\text{obs}_k}, p_{\text{mod}_i}) \quad (12)$$

where

$$l(a, b) = \begin{cases} 1, & b \leq a \\ 0, & \text{otherwise} \end{cases} \quad (13)$$

In practice we slightly ‘soften’ the treatment of limits in the case where $p_{\text{obs}_k} < p_{\text{mod}_i}$ to take into account that no limit is absolute; thus model data points with $p_{\text{mod}_i} > p_{\text{obs}_k}$ are assigned a non-zero probability, again based on a normal distribution, so as to treat the limits as though they were 3σ upper limits. This approach is exactly valid for the limits on core prominences and an adequate approximation for the less well-defined jet limits.

A two- to five- dimensional parameter space is defined by the possible parameters given in Section 3.4.4. The procedure described above effectively integrates over θ and the posterior probability represents a joint posterior probability for some or all of \bar{p}_{int} , $\sigma_{p_{\text{int}}}$, $\bar{\gamma}$, σ_{γ} , γ_{\min} , γ_{\max} or a , depending on how the parameter space has been defined. We are more interested in the posterior probability of some of these parameters than of others: in particular the one of most physical interest is γ . The *marginal* posterior probability of γ , or in general of any other parameter, can be determined from the joint posterior probability by integrating over the other parameters:

$$P(\bar{\gamma} | p_{\text{obs}}, M) = \int dX P(\bar{\gamma}, X | p_{\text{obs}}, M) \quad (14)$$

where X represents all parameters except $\bar{\gamma}$. This integration can be carried out trivially using the output of the MCMC routine.

3.4.6 The evidence and the Bayes factor

The denominator of equation (5) is the ‘evidence’ and is calculated from the following.

$$P(p_{\text{obs}}|I) = \sum_i P(p_{\text{mod}_i}|I)P(p_{\text{obs}}|p_{\text{mod}_i}, I) \quad (15)$$

Since this is the same for each p_{mod_i} for a given model, M , it may be omitted in calculating the posterior probability of p_{mod_i} (equation 5). However, if we want to compare models, for example a model in which we have 2 parameters, $\bar{\gamma}$ and \bar{p}_{int} , with one where we have four, $\bar{\gamma}$, \bar{p}_{int} , σ_γ and $\sigma_{p_{\text{int}}}$, the evidence must be evaluated. This is not possible using only the post burn-in samples from the posterior, as these are, by definition, not uniformly sampled over the prior. Instead, it is possible to use the burn-in samples themselves, as justified by the following.

The continuous equivalent of equation (15) gives us the global likelihood for M , that is the weighted average likelihood for its parameters.

$$P(p_{\text{obs}}|M) = \int dX P(X|I)P(p_{\text{obs}}|X, M) \quad (16)$$

where X represents all parameters.

Remembering that the function actually being sampled by the code is a modification of $P(X|p_{\text{obs}}, I)$, (equation 10), we can define a partition function, $Z(\lambda)$ as

$$\begin{aligned} Z(\lambda) &= \int dX P(X|M, I)P(p_{\text{obs}}|X, M, I)^\lambda \quad (17) \\ &= \int dX \exp\{\ln[P(X|M, I)] + \lambda \ln[P(p_{\text{obs}}|X, M, I)]\} \quad (18) \end{aligned}$$

$Z(\lambda)$ is then the tempering simulation corresponding to λ , and integrating over all λ gives us the function we want, the global likelihood,

$$P(p_{\text{obs}}|M) = \int_0^1 d\ln Z(\lambda) \quad (19)$$

But, from equation (18) with some rearrangement, we can write the derivative of $\ln[Z(\lambda)]$ as

$$\frac{d}{d\lambda} \ln[Z(\lambda)] = \langle \ln[P(p_{\text{obs}}|M, X, I)] \rangle_\lambda \quad (20)$$

where $\langle \ln[P(p_{\text{obs}}|M, X, I)] \rangle_\lambda$ is the expectation value of $\ln[P(p_{\text{obs}}|M, X, I)]$ and the subscript λ denotes which tempering simulation the samples correspond to. But we can also say that

$$\ln[P(p_{\text{obs}}|X, M, I)] = \int \lambda \langle \ln[P(p_{\text{obs}}|X, M, I)] \rangle_\lambda \quad (21)$$

$$\approx \frac{1}{i} \sum_i \lambda_i \langle \ln[P(p_{\text{obs}}|X, M, I)] \rangle_{\lambda_i} \quad (22)$$

So for a given model, the log global likelihood can be obtained from the burn-in samples and this, along with the model prior, can be used to evaluate the odds ratio, defined as the ratio of the evidence values for the two models:

$$O_{1,2} = \frac{P(M_1|I) P(p_{\text{obs}}|M_1, I)}{P(M_2|I) P(p_{\text{obs}}|M_2, I)} \quad (23)$$

In this analysis identical priors are applied to the various models tested, so this expression is simplified to the ratio of global likelihoods, known as the Bayes factor. We can then use the odds ratio or, equivalently, the Bayes factor, to attempt to say which of two models provides the best description of the data.

3.4.7 Credible intervals and regions

We define the credible interval on a parameter for a confidence level p as the smallest interval such that the posterior probability of the parameter lying in the interval is p . In one dimension (i.e. integrating over all other parameters, which in the context of the output of the code simply means ignoring their values) there is clearly, provided the posterior probability has a single peak, a unique choice of interval that satisfies this requirement, which can be found by an exhaustive search over the results of the sampler, and which is accurate up to the constraints imposed by the finite sampling of the posterior. In more than one dimension, there is no such obvious choice, and we find an approximation to the credible region by binning the posterior probability distribution (marginalizing out uninteresting parameters), sorting by the probability of each binned element, and taking the first m elements that sum to give the probability p : the credible region is then approximately the region of parameter space enclosing these m grid elements. This procedure has the advantage that if there truly are multiple peaks in the posterior they will be represented correctly: it has the disadvantage that the results may depend on the binning and, in particular, that the binning may have to be quite coarse in order to define a credible region in many dimensions. In what follows we only present credible intervals in one dimension and credible regions in two dimensions.

We note in passing that this definition of the credible interval can (for a very asymmetrical posterior) actually exclude the position of the Bayesian estimate of the parameter, since it corresponds to the mode, while the Bayesian estimate corresponds to the mean; the credible interval is certainly not constrained to lie symmetrically about the mean (in fact it is more likely to be symmetrical about the maximum-likelihood value). This should be borne in mind when interpreting the ‘errors’ that we quote on certain parameters.

3.5 Method verification

3.5.1 Data simulation

Before running the code on real datasets it is necessary to establish whether the Bayesian estimator of the parameters of interest provided by the code (i.e. the mean of the values of that parameter for all post burn-in samples) is really an unbiased estimate of the true value under realistic conditions and whether the uncertainties (credible intervals) on parameters or combinations of parameters are good estimates of the true uncertainty.

This can be done using Monte Carlo simulations (as H99 did for their K-S test model fitting). To do this we simulated a large number (50) of sets of jet data, with parameters chosen to represent a best guess at what resembles the real data most closely. A simulated dataset contained 100 prominence points, each with p_{obs_j} simulated using equation (3).

Initially p_{int_j} was drawn from a Gaussian distribution with $\ln(\bar{p}_{\text{int}}) = -7$, $\sigma_{p_{\text{int}}} = 0.6$ and we used $\bar{\gamma} = 1.5$, $\sigma_\gamma = 0$. For 30 per cent of sources p_{obs_j} was not used as calculated but instead an upper limit was generated. To generate the upper limits we used a random number between 0.1 and the calculated jet prominence value. While the non-detection of a jet might be expected to be dependent on p_{obs_j} to some extent, when we considered the jet prominences and upper limits for the sample as a whole (Paper I) we found that there was no discernible trend with prominence with respect to upper limits. It would appear that observational effects, particularly the variations in observing resolution, mask any

strong dependence of jet detection on p_{obs_j} such that there is no obvious model that should be used for generating upper limits; hence we adopt a random deviate method. It is reasonable to expect that this method, along with the high maximum upper limit relative to the observed upper limit values used, will only provide simulated data of ‘worse’ quality than that which is observed, justifying the simplifying approach in this context. For the remaining sources, the jet prominence was used with an associated error. This error was drawn from a normal distribution where the mean was the calculated p_{obs_j} and the standard deviation was variable, itself taken from a normal distribution with $(0, 0.1 \times p_j)$. This standard deviation was chosen to simulate as closely as possible the error distribution of the real jet data.

3.5.2 Parameter estimation

For each simulated dataset we then ran the MCMC code and derived the posterior probability distribution, from which we could obtain the Bayesian estimators of the value of each parameter. The mean and dispersion of the values of $\langle \bar{\gamma} \rangle$, $\langle \ln(\bar{p}_{\text{int}}) \rangle$ and $\langle \sigma_{p_{\text{int}}} \rangle$ for each run of the code – where the angle brackets denote the Bayesian estimates of the model parameters – then tell us whether the code recovers the true values and estimates the uncertainties appropriately. For the initial trial input values of $\bar{\gamma}$ and $\ln(\bar{p})$ we obtained a mean $\langle \bar{\gamma} \rangle$ of 1.52 and a standard deviation of 0.14, a mean $\langle \ln(\bar{p}_{\text{int}}) \rangle$ of -7.01 with standard deviation 0.16 and a mean $\langle \sigma_{p_{\text{int}}} \rangle$ of 0.56 with standard deviation 0.16. We can see that while the errors and limits imposed on the data result in considerable scatter in the returned parameters about the true (input) values, the means are in good agreement with those true values once the scatter is taken into account. Thus there is no evidence that the code is biased for this type of dataset. Moreover, the standard deviations we find (which are in some sense frequentist estimates of the uncertainties on the fitting procedure, and were used in that way by H99) are very similar in magnitude to the credible intervals inferred from the posterior probability distributions for individual simulations. We verified that the same result holds for a range of other values of $\bar{\gamma}$. The fitting procedure is, unsurprisingly, biased if we fit the wrong model (e.g., if we fit a simulated dataset with intrinsic dispersion with a model in which $\sigma_{p_{\text{int}}}$ is held at zero, then we will recover an artificially high value of $\bar{\gamma}$) but for models that match the data it is not. This is true for all parameters of the basic model and also for the parameters of the power-law model for cores when we carried out appropriate simulations, although we noted in simulating power-law distributions that it is very hard to recover good constraints on γ_{max} , which is only constrained by the tail of the prominence distribution.

3.5.3 Model selection

We further investigated whether the Bayesian evidence could reliably be used to distinguish between models. Again concentrating on simulated datasets with σ_γ set to zero and with properties matched to the observed jet data, we simulated a large number of datasets with $\sigma_{p_{\text{int}}} > 0$ and investigated whether the Bayes factor allowed us to distinguish between models in which (a) the fitted $\sigma_{p_{\text{int}}}$ was fixed to zero and (b) it was allowed to vary. The results turned out to depend on the value of $\sigma_{p_{\text{int}}}$ adopted in the simulated data, as one would expect. For very low values of the simulated $\sigma_{p_{\text{int}}}$, the Bayes factor on average favoured the simpler model, even though it is formally incorrect: the data here simply do not give us

enough information to require the extra parameter. For larger values of the input $\sigma_{p_{\text{int}}}$, $\gtrsim 0.2$, the Bayes factor clearly tends to favour the models with non-zero intrinsic dispersion. However, when we fitted the same data with other versions of the basic model with intrinsic dispersion (e.g. models where $\sigma_{p_{\text{int}}}$ was constrained to be zero and σ_γ was allowed to vary) we found that the Bayes factor did not reliably distinguish between the correct model and other possible models for the dispersion; all such models gave very similar Bayes factors. Consistent with this, we found that the Bayes factor in simulations did not allow us to distinguish between versions of the basic model with Gaussian dispersion either in the intrinsic prominence or in the Lorentz factor and the power-law model for cores; again, the Bayes factor is sufficient to point to some dispersion but not to say what its origin is.

3.5.4 Observed data

Finally we note that two factors distinguish the jet and core data. The core data contains far fewer upper limits than the jet data and so in one sense is expected to be easier to fit. However, as is evident from the broader distribution of core prominences (Fig. 2) and also expected from earlier work (e.g. H99) we expect significantly larger $\bar{\gamma}$ values in the fits to the cores. This means that the feature of the data that discriminates between different models becomes the extent of the tail of very high prominences. However, since there are only a very few sources with such high values, the fit becomes less reliable. In a fit to 50 simulated jet data sets with input $\bar{\gamma} = 5.0$ and $\sigma_{p_{\text{int}}} = 0.6$, we found a mean fitted $\bar{\gamma}$ of 5.3 with standard deviation 1.0. The higher standard deviation of the fit results to the simulated data as a fraction of the true γ , when compared to the jet data, indicates that the second factor dominates: even though the core data are in some sense better, the fitting problem is harder and the results likely to be more uncertain.

We conclude that the MCMC fitting procedure can give a good estimate of the true underlying beaming parameters in the presence of the types of error and the numbers of upper limits seen in the real data. In the next section we proceed to use this procedure to estimate parameters using the actual measurements.

4 RESULTS

4.1 Jets

Since the spectral indices of jets are poorly known, we carried out all the modelling in this section for two representative values of jet spectral index, $\alpha = 0.5$ and $\alpha = 0.8$ (recalculating the jet prominence distribution consistently for the $\alpha = 0.8$ case from the original data of Paper I.) By using these two values, which are close to the extreme values observed for individual objects, we can both evaluate the extent to which a choice of α affects our results and, hopefully, bracket the true values of the beaming parameters for intermediate spectral index values.

We initially used the simplest possible model, with an assumed delta-function distribution in both the intrinsic prominence and the bulk Lorentz factor, to estimate beaming parameters from the prominence distribution of the jets for all 98 objects in the sample. We then allowed the parameters governing the intrinsic dispersion in prominence and Lorentz factor to vary. Results are shown in Fig. 3 (for the $\alpha = 0.5$ case) and tabulated in Table 2. (It should be noted that the posterior distribution of σ_γ is clearly limited by

the prior: the upper limit on the prior distribution was chosen so as to avoid generating large numbers of negative Lorentz factors.)

Comparison of the values for the different α values in Table 2 shows that, as expected, the choice of jet spectral index has a significant effect on the result. Although the two sets of results are very comparable, the results for the higher spectral index have systematically lower estimated Lorentz factors. The next thing to note is that the Lorentz factor for a delta-function distribution in both parameters is quite high: $\bar{\gamma} = 2.37$ corresponds to $\beta = 0.91$, and $\bar{\gamma} = 2.07$ to $\beta = 0.88$, which can be compared to the $\beta = 0.62$ found by H99. However, when we allow any dispersion in either the intrinsic prominence or the Lorentz factor, the values of $\bar{\gamma}$ drop very substantially. $\bar{\gamma} = 1.28$ corresponds to $\beta = 0.62$ and 1.18 to $\beta = 0.53$; H99 found $\beta \approx 0.5$ for a similar model. We emphasise that no model allows jet speeds with $\gamma \sim 10$; this would predict a much larger dispersion than is seen in the data. The ratios of evidence (Bayes factors) very strongly favour any model with intrinsic dispersion, but does not allow us to distinguish between the three different models that have this property with any degree of confidence (as we would expect from the simulations discussed above). In fact, when we fitted a model with $\bar{\gamma}$ fixed to 1.0 and $\sigma_\gamma = 0$ (i.e. the data are modelled with *only* a lognormal prominence distribution) the Bayes factor marginally favours this simplest model over any other, showing that the prominence data in themselves provide no evidence for a beaming model, while intrinsic scatter in the data is required.

Since there is some evidence that the low-excitation radio galaxies (LERGs) do not participate in the unified models for narrow-line radio galaxies, broad-line radio galaxies and quasars (see H99 for details) we also fitted the same set of models to the prominence data excluding the 15 low-excitation objects in the sample. The very similar results we obtained are tabulated in Table 2. As the inclusion or exclusion of the small number of LERGs clearly makes little difference to the results, we do not show plots of the posterior probability distribution.

4.2 Luminosity dependence in jets

As mentioned above (Section 4.1), our best estimates of γ for jet models either with or without intrinsic dispersion tend to lie above the corresponding values found by H99. To some extent this is expected, since (i) we take limits and errors into account properly, which H99's method did not permit, and a correct treatment of the limits at least would be expected to broaden the effective distribution, and (ii) we are quoting not the maximum-likelihood value but the Bayesian estimator of the Lorentz factor, $\int \gamma p(\gamma) d\gamma$, which will be biased towards higher values with respect to the maximum-likelihood estimator if $p(\gamma)$ has a long tail to higher values, as it undoubtedly does in some fits (Fig. 3). In addition, H99 used a different definition of prominence, normalizing with respect to the total high-frequency flux, which might have tended to reduce the scatter in the observed prominence if any of the high-frequency structure (e.g. hotspots) had been affected by beaming.

However, it is worth asking whether any component of this difference could correspond to a real physical difference between our sample and that of H99. The two samples overlap to some extent – of the 31 NLRG studied by H99, 22 are also in our sample – but the main difference is that H99 considered only objects with $z < 0.3$, and hence largely with low luminosities. We began our investigation by fitting our models with $\sigma_{p_{\text{int}}} = 0$ and $\sigma_\gamma = 0$ to the jet data of H99, for consistency treating upper limits as detections and assuming a constant fractional error on each prominence mea-

surement. For consistency with the convention adopted by H99, we use $\alpha = 0.8$ throughout this comparison. We found a Bayesian estimate of $\bar{\gamma} = 1.65^{+0.01}_{-0.07}$ ($\beta = 0.80$), which is considerably larger than the best-fitting value found by H99, $\beta = 0.62$. This suggests that there is some difference in the different fitting approaches, and perhaps reinforces the notion that H99's approach of fitting using the K-S statistic was not ideal. If we allow $\sigma_{p_{\text{int}}}$ to vary in the fits, which was the most sophisticated model considered by H99, we obtain $\bar{\gamma} = 1.10^{+0.02}_{-0.07}$; this corresponds to $\beta = 0.43$, which is very similar to the $\beta \approx 0.5$ reported by H99.

Although this is at best qualified success in reproducing the results of H99, we noted that the values of γ for the two models we fitted lay systematically below the results we obtained for fitting the same models to our sample as a whole (Section 4.1, Table 2). This motivated us to look for luminosity effects in the jet speeds in our sample. For simplicity we divided the whole sample, including LERGs, at a 178-MHz luminosity of $5 \times 10^{26} \text{ W Hz}^{-1} \text{ sr}^{-1}$, which is the cutoff luminosity we used in a number of statistical tests in Paper I. This gives a sample of 40 low-luminosity and 58 high-luminosity objects. When we fitted the model with $\sigma_{p_{\text{int}}} = 0$ and $\sigma_\gamma = 0$ to these two datasets (here using $\alpha = 0.5$ only), we found that $\bar{\gamma} = 2.37^{+0.09}_{-0.28}$ for the low-luminosity sample and $1.92^{+0.03}_{-0.09}$ for the high-luminosity one, a marginally significant difference but one that is in the *opposite* sense to that implied by the results above from the H99 data. When we fitted the model with $\sigma_\gamma = 0$ but $\sigma_{p_{\text{int}}}$ free, we found $\bar{\gamma} = 1.25^{+0.06}_{-0.21}$ for the low-luminosity sample and $1.55^{+0.12}_{-0.14}$ for the high-luminosity one. However, the intrinsic dispersion for the low-luminosity sample is higher ($\sigma_{p_{\text{int}}} = 1.04^{+0.11}_{-0.12}$ versus $0.65^{+0.13}_{-0.17}$) so it is plausible that we are simply seeing different tradeoffs in the somewhat degenerate plane of γ versus $\sigma_{p_{\text{int}}}$. If, finally, we fix $\sigma_{p_{\text{int}}}$ to its best-fitting value of 0.95 for the whole sample (Table 2) and repeat the fits, the estimates of γ become $1.29^{+0.08}_{-0.18}$ and $1.33^{+0.11}_{-0.16}$ respectively; these are not significantly different from each other or from the estimate for the sample as a whole. We conclude that there is no convincing evidence for a trend in $\bar{\gamma}_j$ with source luminosity.

4.3 Cores

Using the basic model, we find that, for a delta-function distribution in Lorentz factor and intrinsic prominence, \bar{p}_{int} and $\bar{\gamma}$ are constrained to lie along a line in parameter space, as found in previous work (see Hardcastle et al. 2003 for the equation of this line) and we can only really say that $\bar{\gamma} \gtrsim 10$ (the limit $\bar{\gamma} < 20$ is imposed by the prior). However, when any intrinsic dispersion is introduced, $\bar{\gamma}$ becomes reasonably well constrained, with Bayesian estimators in the range 10–14, though again this is affected by the choice of prior. As in the case of the jets, the Bayes factors for these models strongly favour some intrinsic dispersion, but we cannot distinguish between different dispersion models. Models with no beaming and only intrinsic dispersion are not favoured in this dataset, presumably because the tail of the prominence distribution is not well modelled with a lognormal distribution.

Again, we also fitted the same set of models to the subsample that excludes the LERGs. Here the tendency is to reduce the values of $\bar{\gamma}$ required – perhaps because the LERGs include a significant number of both core non-detections with strong upper limits and bright cores with high prominence values. The results of fitting the basic model to both datasets are tabulated in Table 3.

We then estimated the parameters of the power-law model for the core prominence distribution. These results are tabulated in Table 4. We initially fixed $\sigma_{p_{\text{int}}}$ to 0, so that all the dispersion

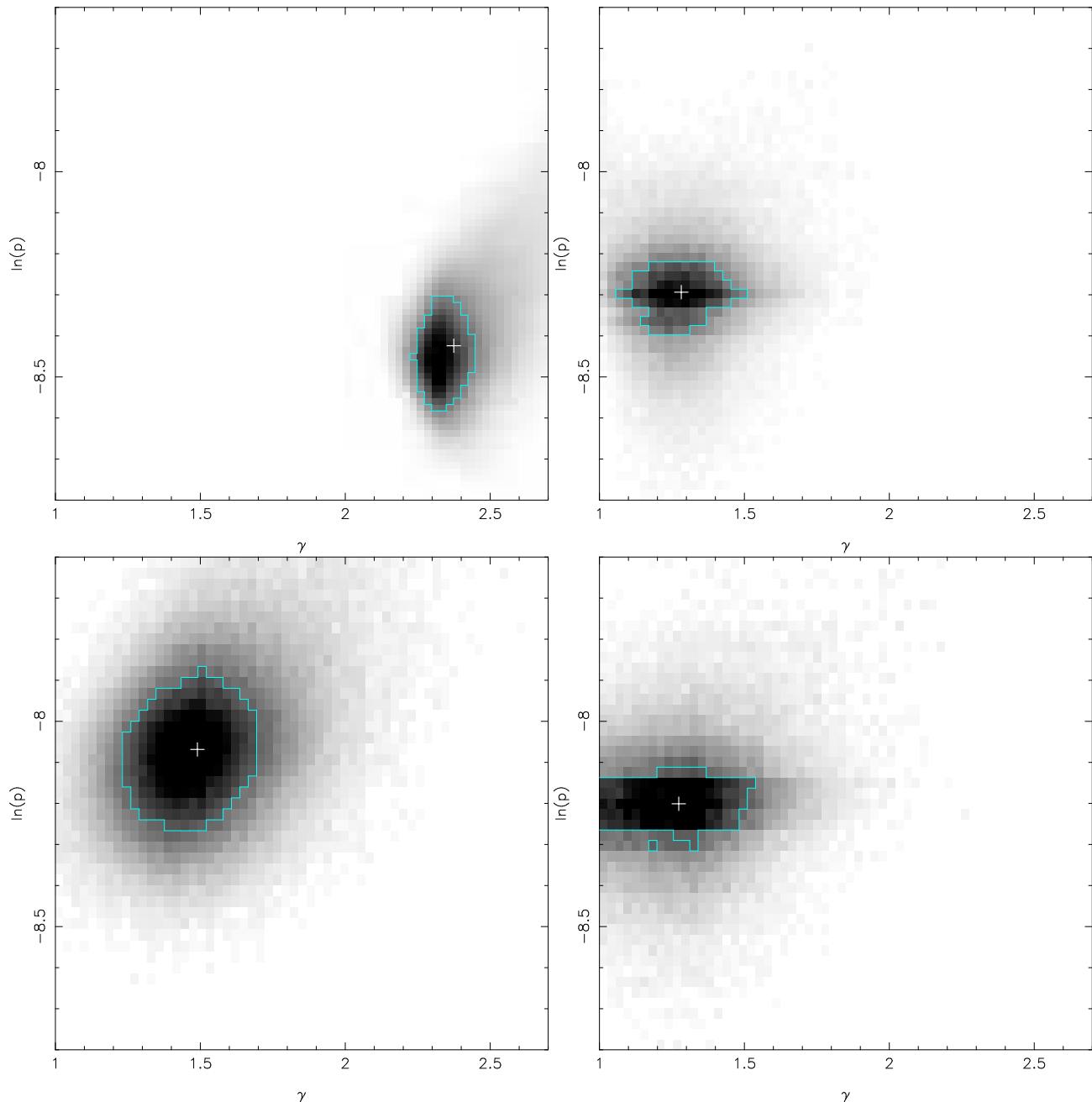


Figure 3. The posterior probability distribution for fits to the jet prominence distribution for the whole sample. Contours show the smallest region that contains 68 per cent of the posterior probability distribution, i.e. the two-dimensional Bayesian credible region as defined in Section 3.4.7. The white cross marks the position of the Bayesian estimator of p_{int} and γ . Top left: a delta-function distribution is assumed for both the intrinsic prominence and the Lorentz factor (i.e. $\sigma_\gamma = 0$, $\sigma_{p_{\text{int}}} = 0$). Top right: $\sigma_\gamma = 0$ but $\sigma_{p_{\text{int}}}$ is allowed to vary. Bottom left: $\sigma_{p_{\text{int}}} = 0$ but σ_γ is allowed to vary. Bottom right: both $\sigma_{p_{\text{int}}}$ and σ_γ are allowed to vary. All plots are marginalized over $\sigma_{p_{\text{int}}}$ and σ_γ for ease of comparison.

comes from the power-law distribution of γ ; with this prior we obtain some constraints on the remaining parameters of the model, though they are still strongly affected by the choice of prior (particularly γ_{max} , which we expect from the simulated data to be unconstrained). We attempted a fit with a fixed a value of 2.0, as favoured by some previous work (e.g. Liu & Zhang 2007) but this is strongly disfavoured by the Bayes factor. When $\sigma_{p_{\text{int}}}$ is free, the parameters of the power-law model are essentially unconstrained, although the Bayes factor favours such a model. It can be seen that, as expected from the simulations, these data give us no reason to

favour a power-law distribution of Lorentz factors over a lognormal one; the very slight difference in Bayes factors in favour of the power-law model when $\sigma_{p_{\text{int}}}$ is free is not significant.

4.4 Luminosity dependence in cores

In Paper I, we suggested that the statistically significant difference in core prominence seen in our low-luminosity and high-luminosity samples might be evidence for a dependence of Lorentz factor on source luminosity. To investigate this we divided the

Table 2. Results of fits to the jet prominence distribution. Fits are carried out for two values of the assumed jet spectral index, α . The Bayes factor quoted is the natural log of the ratio between the evidence value for the $\sigma_\gamma = 0, \sigma_{p_{\text{int}}} = 0$ fit (for a given sample and α) and the others; thus it gives a measure of the degree to which the other fits are preferred. Errors quoted are 68 per cent credible intervals marginalizing over all other parameters. Where no errors are quoted, the quantity concerned was fixed at the stated level.

Sample	α	Model	$\bar{\gamma}$	$\ln(\bar{p}_{\text{int}})$	$\sigma_{p_{\text{int}}}$	σ_γ	Bayes factor
Jets, all sources	0.5	$\sigma_\gamma = 0, \sigma_{p_{\text{int}}} = 0$	$2.37^{+0.03}_{-0.11}$	$-8.42^{+0.06}_{-0.11}$	0	0	–
		$\sigma_\gamma = 0, \sigma_{p_{\text{int}}}$ free	$1.28^{+0.10}_{-0.11}$	$-8.29^{+0.06}_{-0.05}$	$0.95^{+0.10}_{-0.09}$	0	19.4
		σ_γ free, $\sigma_{p_{\text{int}}} = 0$	$1.49^{+0.12}_{-0.17}$	$-8.07^{+0.12}_{-0.13}$	0	$0.46^{+0.12}_{-0.05}$	20.0
		σ_γ free, $\sigma_{p_{\text{int}}}$ free	$1.27^{+0.13}_{-0.18}$	$-8.20^{+0.06}_{-0.06}$	$0.76^{+0.15}_{-0.13}$	$0.30^{+0.18}_{-0.15}$	19.5
		$\bar{\gamma} = 1.0, \sigma_\gamma = 0, \sigma_{p_{\text{int}}}$ free	1.0	$-7.91^{+0.11}_{-0.10}$	$1.18^{+0.05}_{-0.06}$	0	21.0
	0.8	$\sigma_\gamma = 0, \sigma_{p_{\text{int}}} = 0$	$2.07^{+0.02}_{-0.06}$	$-8.50^{+0.05}_{-0.09}$	0	0	–
		$\sigma_\gamma = 0, \sigma_{p_{\text{int}}}$ free	$1.18^{+0.05}_{-0.07}$	$-8.36^{+0.08}_{-0.03}$	$0.94^{+0.08}_{-0.07}$	0	19.2
		σ_γ free, $\sigma_{p_{\text{int}}} = 0$	$1.24^{+0.09}_{-0.15}$	$-8.18^{+0.10}_{-0.10}$	0	$0.45^{+0.11}_{-0.06}$	20.2
		σ_γ free, $\sigma_{p_{\text{int}}}$ free	$1.16^{+0.04}_{-0.16}$	$-8.25^{+0.06}_{-0.07}$	$0.64^{+0.19}_{-0.15}$	$0.32^{+0.15}_{-0.13}$	19.3
		$\bar{\gamma} = 1.0, \sigma_\gamma = 0, \sigma_{p_{\text{int}}}$ free	1.0	$-7.90^{+0.11}_{-0.09}$	$1.11^{+0.04}_{-0.06}$	0	21.0
Jets, LERGs excluded	0.5	$\sigma_\gamma = 0, \sigma_{p_{\text{int}}} = 0$	$2.43^{+0.04}_{-0.14}$	$-8.42^{+0.07}_{-0.13}$	0	0	–
		$\sigma_\gamma = 0, \sigma_{p_{\text{int}}}$ free	$1.32^{+0.11}_{-0.12}$	$-8.35^{+0.07}_{-0.06}$	$0.94^{+0.09}_{-0.11}$	0	14.4
		σ_γ free, $\sigma_{p_{\text{int}}} = 0$	$1.51^{+0.14}_{-0.13}$	$-8.12^{+0.12}_{-0.14}$	0	$0.46^{+0.14}_{-0.09}$	15.6
		σ_γ free, $\sigma_{p_{\text{int}}}$ free	$1.31^{+0.13}_{-0.19}$	$-8.24^{+0.06}_{-0.07}$	$0.73^{+0.18}_{-0.13}$	$0.32^{+0.14}_{-0.14}$	14.5
		$\bar{\gamma} = 1.0, \sigma_\gamma = 0, \sigma_{p_{\text{int}}}$ free	1.0	$-7.97^{+0.07}_{-0.05}$	$1.19^{+0.05}_{-0.05}$	0	15.8
	0.8	$\sigma_\gamma = 0, \sigma_{p_{\text{int}}} = 0$	$2.11^{+0.02}_{-0.08}$	$-8.50^{+0.06}_{-0.11}$	0	0	–
		$\sigma_\gamma = 0, \sigma_{p_{\text{int}}}$ free	$1.21^{+0.06}_{-0.10}$	$-8.38^{+0.06}_{-0.06}$	0	$0.97^{+0.11}_{-0.07}$	15.6
		σ_γ free, $\sigma_{p_{\text{int}}} = 0$	$1.30^{+0.12}_{-0.15}$	$-8.20^{+0.13}_{-0.11}$	0	$0.45^{+0.13}_{-0.06}$	15.4
		σ_γ free, $\sigma_{p_{\text{int}}}$ free	$1.20^{+0.09}_{-0.16}$	$-8.26^{+0.04}_{-0.06}$	$0.61^{+0.24}_{-0.17}$	$0.34^{+0.16}_{-0.12}$	14.0
		$\bar{\gamma} = 1.0, \sigma_\gamma = 0, \sigma_{p_{\text{int}}}$ free	1.0	$-7.94^{+0.05}_{-0.06}$	$1.15^{+0.03}_{-0.06}$	0	15.5

sample of core prominences by luminosity in the same way as was done for jets in Section 4.2. Fitting only the version of the basic model in which $\sigma_{p_{\text{int}}}$ is free, since, as discussed above, only models with some intrinsic dispersion give reasonably well-constrained $\bar{\gamma}$ values, we found $\bar{\gamma} = 11.20^{+4.87}_{-5.66}$ for the low-luminosity sources and $10.67^{+3.51}_{-6.43}$ for the high-luminosity sources. Thus there is no evidence for differences in Lorentz factor, although clearly $\bar{\gamma}$ is poorly constrained. The intrinsic normalization values for the low- and high-luminosity sample are respectively $-4.70^{+1.26}_{-0.55}$ and $-6.06^{+1.21}_{-0.84}$, while the estimates of $\sigma_{p_{\text{int}}}$ are $1.40^{+0.15}_{-0.24}$ and $1.19^{+0.14}_{-0.23}$. The most obvious interpretation of these results is that, if any luminosity dependence is present in our data, it is a luminosity dependence of intrinsic prominence rather than of bulk Lorentz factor; either explanation is of course equally good in terms of reproducing our original observation of a difference in observed prominence. Given these results and the fact that in any case the data do not appear to allow us to distinguish between any but the simplest of models for core Lorentz factor distribution, we have not attempted to fit a model in which core Lorentz factor depends on source luminosity to the data.

4.5 Core-jet correlation

Fits to the jet and core prominence distributions alone do not take into account the correlation between the two quantities. In a model in which the prominence distributions were completely dominated by intrinsic scatter, we would expect no correlation between these two quantities, but in fact we showed in Paper I that there is such a correlation which is significant even in the presence of upper limits. It is straightforward to modify our approach to simulate the two-dimensional probability distribution of jet and core prominences and to sum the likelihoods of objects in (jet, core) prominence space. Accordingly we carried out some fits using this approach, fitting, as before, both to the full database and to the subset of sources that excludes the LERGs. Since we have seen that intrinsic

dispersion is required in the fits to the two quantities individually, we included this in our two-dimensional models; for simplicity we restricted ourselves to a model in which there are intrinsic dispersions in the prominences but not in the beaming speeds, so that the free parameters of the model are $\bar{p}_{\text{int}c}, \sigma_{p_{\text{int}c}}, \bar{\gamma}_c, \bar{p}_{\text{int}j}, \sigma_{p_{\text{int}j}}$ and $\bar{\gamma}_j$.

Results of these fits are tabulated in Table 5, again allowing the jet spectral index to be either 0.5 or 0.8, and an example of the posterior probability distribution for the beaming parameters is shown in Fig. 5. It can be seen that beaming is strongly required by the Bayes factor between these models and the corresponding ones in which the Lorentz factors are fixed to 1.0, as we might expect. The effect of including the core-jet correlation in the modelling is to make less probable the regions of parameter space with no beaming (compare the right-hand panel of Fig. 5 with the top right-hand panel of Fig. 3). The Bayesian estimates of the beaming speeds are therefore slightly higher than in the case where the correlation is not taken into account ($\bar{\gamma}_j = 1.35$ corresponds to $\beta_j = 0.67$, and $\bar{\gamma}_j = 1.23$ to $\beta_j \approx 0.58$) although there is substantial overlap in the credible intervals. Once again, there is little difference between the results for all sources and the results that exclude the LERGs.

5 DISCUSSION AND CONCLUSIONS

The models for the prominences of both jets and cores are a function of three variables, $(p_{\text{int}}, \gamma, \theta)$, so that the problem of fitting to the γ distribution is degenerate. However, as discussed in Section 3.4.1, prominence distributions simulated using these models do represent the sample data well, and are strongly influenced by the value of γ . The model fitting that we have performed in this paper has allowed the upper limits in the data to be treated correctly and so the following conclusions can be drawn about the probable range of γ in the jet and core data.

For both jets and cores, it was found that models allowing

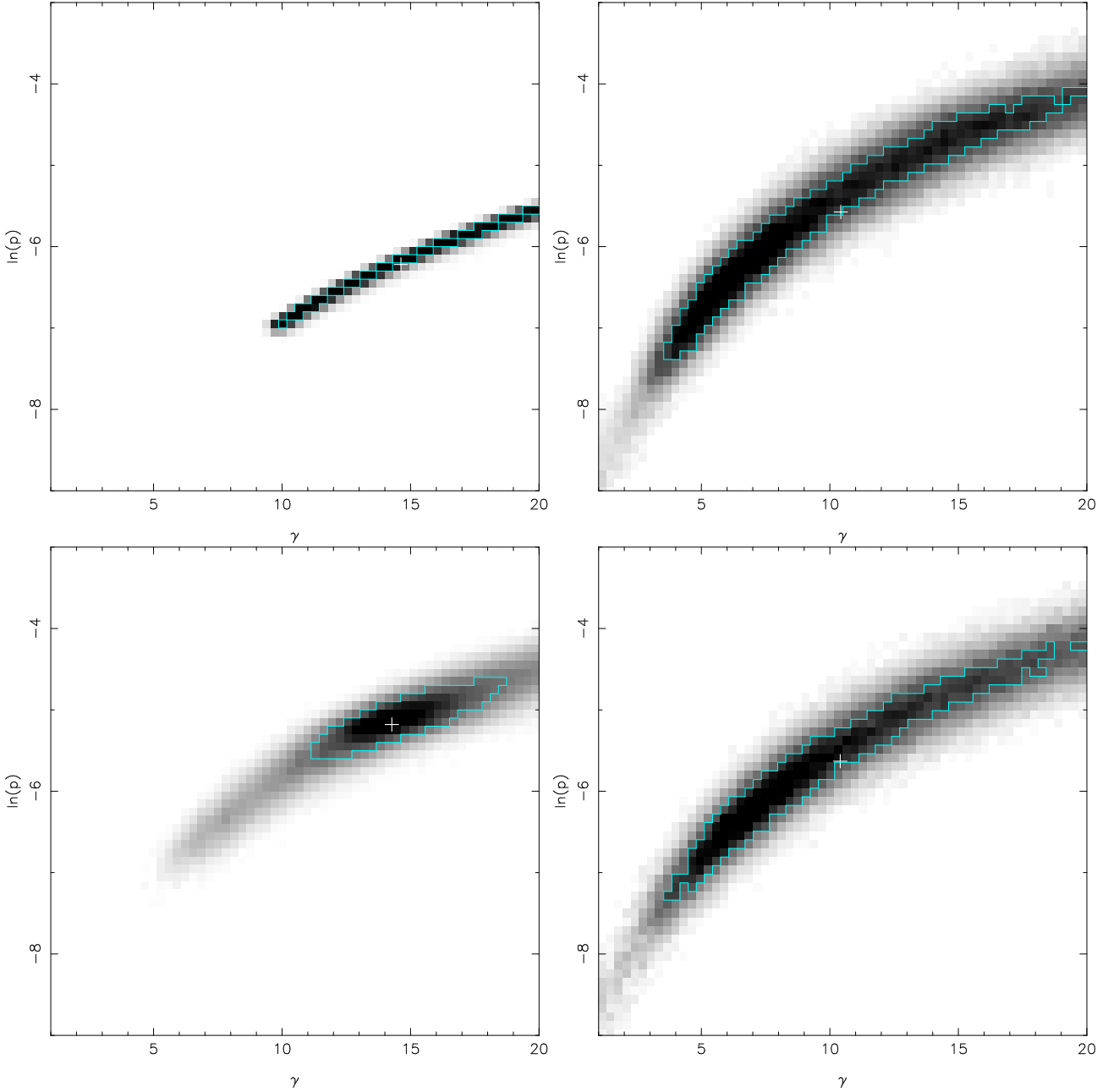


Figure 4. The posterior probability distribution for fits to the core prominence distribution. Labelling as for Fig. 3. Top left: a delta-function distribution is assumed for both the intrinsic prominence and the Lorentz factor (i.e. $\sigma_\gamma = 0$, $\sigma_{p_{\text{int}}} = 0$). Top right: $\sigma_\gamma = 0$ but $\sigma_{p_{\text{int}}}$ is allowed to vary. Bottom left: $\sigma_{p_{\text{int}}} = 0$ but σ_γ is allowed to vary. Bottom right: both $\sigma_{p_{\text{int}}}$ and σ_γ are allowed to vary. All plots are marginalized over $\sigma_{p_{\text{int}}}$ and σ_γ for ease of comparison.

Table 3. Results of fits of the basic model to the core prominence distribution. Conventions as for Table 2.

Sample	Model	$\bar{\gamma}$	$\ln(\bar{p}_{\text{int}})$	$\sigma_{p_{\text{int}}}$	σ_γ	Bayes factor
Cores, all sources	$\sigma_\gamma = 0$, $\sigma_{p_{\text{int}}} = 0$	$14.62^{+2.02}_{-4.71}$	$-6.22^{+0.65}_{-0.28}$	0	0	–
	$\sigma_\gamma = 0$, $\sigma_{p_{\text{int}}}$ free	$10.42^{+3.15}_{-6.54}$	$-5.57^{+1.31}_{-0.72}$	$1.43^{+0.12}_{-0.13}$	0	33.6
	σ_γ free, $\sigma_{p_{\text{int}}} = 0$	$14.27^{+2.58}_{-2.44}$	$-5.18^{+0.40}_{-0.24}$	0	$0.57^{+0.03}_{-0.01}$	32.9
	σ_γ free, $\sigma_{p_{\text{int}}}$ free	$10.40^{+3.03}_{-5.91}$	$-5.63^{+1.02}_{-0.84}$	$1.23^{+0.21}_{-0.17}$	$0.33^{+0.27}_{-0.09}$	33.7
	$\bar{\gamma} = 1.0$, $\sigma_\gamma = 0$, $\sigma_{p_{\text{int}}}$ free	1.0	$-8.68^{+0.11}_{-0.12}$	$2.15^{+0.09}_{-0.11}$	0	32.7
Cores, LERGs excluded	$\sigma_\gamma = 0$, $\sigma_{p_{\text{int}}} = 0$	$11.96^{+2.75}_{-6.39}$	$-6.69^{+1.17}_{-0.93}$	0	0	–
	$\sigma_\gamma = 0$, $\sigma_{p_{\text{int}}}$ free	$8.24^{+2.39}_{-5.46}$	$-6.28^{+0.93}_{-1.45}$	$1.31^{+0.11}_{-0.16}$	0	27.8
	σ_γ free, $\sigma_{p_{\text{int}}} = 0$	$12.66^{+5.67}_{-2.82}$	$-5.52^{+0.91}_{-0.28}$	0	$0.55^{+0.05}_{-0.01}$	27.9
	σ_γ free, $\sigma_{p_{\text{int}}}$ free	$8.84^{+2.49}_{-5.64}$	$-6.13^{+1.03}_{-1.16}$	$1.09^{+0.22}_{-0.21}$	$0.34^{+0.26}_{-0.08}$	28.0
	$\bar{\gamma} = 1.0$, $\sigma_\gamma = 0$, $\sigma_{p_{\text{int}}}$ free	1.0	$-8.80^{+0.11}_{-0.10}$	$2.02^{+0.09}_{-0.08}$	0	27.8

Table 4. Results of fits of the power-law model to the core prominence distribution. Conventions as for Table 2. The Bayes factor is with respect to the corresponding model with $\sigma_\gamma = 0$, $\sigma_{p_{\text{int}}} = 0$ in Table 3.

Sample	Model	$\ln(\bar{p}_{\text{int}})$	$\sigma_{p_{\text{int}}}$	γ_{min}	γ_{max}	a	Bayes factor
Cores, all sources	$\sigma_{p_{\text{int}}} = 0, a$ free	$-6.10^{+0.34}_{-0.23}$	0	$4.11^{+0.89}_{-0.25}$	$30.74^{+8.16}_{-3.83}$	$0.15^{+0.02}_{-0.15}$	31.1
	$\sigma_{p_{\text{int}}} = 0, a = 2$	$-3.12^{+0.76}_{-0.26}$	0	$2.49^{+0.49}_{-1.49}$	$29.46^{+10.83}_{-2.99}$	2	24.0
	$\sigma_{p_{\text{int}}}$ free, a free	$-6.77^{+0.47}_{-0.35}$	$1.40^{+0.21}_{-0.23}$	$3.77^{+1.17}_{-0.38}$	$24.24^{+5.29}_{-14.13}$	$2.60^{+2.09}_{-1.10}$	35.0
Cores, LERGs excluded	$\sigma_{p_{\text{int}}} = 0, a$ free	$-6.74^{+0.29}_{-0.34}$	0	$3.47^{+0.43}_{-0.69}$	$26.56^{+7.02}_{-8.79}$	$0.43^{+0.07}_{-0.42}$	26.9
	$\sigma_{p_{\text{int}}} = 0, a = 2$	$-7.07^{+0.20}_{-0.26}$	0	$3.90^{+0.41}_{-0.53}$	$28.12^{+11.87}_{-3.95}$	2	24.1
	$\sigma_{p_{\text{int}}}$ free, a free	$-7.10^{+0.48}_{-0.40}$	$1.21^{+0.25}_{-0.27}$	$3.44^{+0.78}_{-0.89}$	$24.35^{+5.29}_{-14.35}$	$2.63^{+2.31}_{-0.85}$	28.8

Table 5. Results of joint fits to the jet and core prominence distributions for the whole sample for jet spectral indices $\alpha = 0.5$ and $\alpha = 0.8$. Conventions as for Table 2, but the Bayes factor is measured with respect to the model with free beaming parameters.

Sample	α	Model	$\tilde{\gamma}_c$	$\ln(\bar{p}_{\text{int}_c})$	$\sigma_{p_{\text{int}_c}}$	$\tilde{\gamma}_j$	$\ln(\bar{p}_{\text{int}_j})$	$\sigma_{p_{\text{int}_j}}$	Bayes factor
All sources	0.5	All free	$11.81^{+5.37}_{-4.74}$	$-5.17^{+1.10}_{-0.55}$	$1.50^{+0.12}_{-0.14}$	$1.37^{+0.06}_{-0.12}$	$-8.29^{+0.11}_{-0.14}$	$0.97^{+0.09}_{-0.11}$	–
		No beaming	1.0			1.0			–10.0
	0.8	All free	$11.76^{+6.57}_{-3.55}$	$-5.18^{+1.10}_{-0.51}$	$1.49^{+0.09}_{-0.16}$	$1.23^{+0.03}_{-0.08}$	$-8.36^{+0.11}_{-0.10}$	$0.98^{+0.08}_{-0.11}$	–
		No beaming	1.0			1.0			–8.0
LERGs excluded	0.5	All free	$10.49^{+3.56}_{-7.29}$	$-5.61^{+1.55}_{-0.64}$	$1.38^{+0.13}_{-0.12}$	$1.28^{+0.06}_{-0.13}$	$-8.39^{+0.13}_{-0.13}$	$1.07^{+0.06}_{-0.09}$	–
		No beaming	1.0			1.0			–4.0
	0.8	All free	$9.48^{+3.27}_{-6.30}$	$-5.85^{+1.02}_{-1.56}$	$1.39^{+0.09}_{-0.12}$	$1.20^{+0.02}_{-0.05}$	$-8.41^{+0.12}_{-0.12}$	$1.05^{+0.07}_{-0.08}$	–
		No beaming	1.0			1.0			–4.2

some dispersion in one or both of the intrinsic distributions of p_{int} and γ are favoured over the model that assumes a delta-function distribution for both parameters. For the jets, the value of $\tilde{\gamma}$ found for these models varied between 1.18 and 1.49 (see Table 2), depending on the model and the choice of α , which corresponds to $\beta \approx 0.53 - 0.74$ and is in reasonable agreement with previously reported analysis, as discussed in Section 1.1. Models with $\gamma \approx 10$ did not fit well to the data and there was no evidence for any luminosity dependence of $\tilde{\gamma}$. For the cores, a reasonably well constrained $\tilde{\gamma}$ of $\approx 10-14$ was obtained in models in which intrinsic dispersion in the prominence was allowed, but the results here are dependent on our choice of prior.

One obvious criticism of the core data modeling is that it has been assumed that the properties of the twin parsec-scale jets are the same and that the jets are bi-polar. More complicated models could be defined that allow the p_{int} and γ values to be different in the approaching and receding jet, and allow the separation between the jets to be less than 180° – even if the real parsec-scale jets properties are similar or close to being symmetrical in the two beams, it is entirely plausible there is at least some deviation from exact symmetry. Experimenting with such models, however, determined that the data does not justify models any more complex than those reported in the preceding sections and Table 2. That is, the evidence values associated with the models with greater numbers of parameters are not higher and fitting results do not differ greatly from those obtained with the simpler models. Considerably larger datasets will be needed to investigate more complex models.

We also carried out fits to the combined jet and core prominence datasets, as evidence for a jet-core correlation has been found in our sample and in others (Bridle et al. 1994; H99; Paper I). The results showed that models with no beaming are strongly disfavoured with respect to models in which beaming is included, since only the latter can reproduce the observed core-jet correlation. The fitted γ value for the kiloparsec-scale jets was slightly higher than for the corresponding fits in which the correlation was not taken into account – $\gamma_{\text{jet}} = 1.35$, which corresponds to $\beta \approx 0.67$, for $\alpha = 0.5$, or $\gamma_{\text{jet}} = 1.23$, $\beta \approx 0.58$, for $\alpha = 0.8$. Even so, these values, which represent our best estimates in the sense that

they make use of all the available data, are still clearly much lower than 10.

How can these results, implying mildly relativistic bulk speeds for kpc-scale jets in FRIIs, be reconciled with the much larger values of jet bulk Lorentz factor required by beamed inverse-Compton models of X-ray emission from quasar jets (Section 1.1)? As we have already pointed out, jet velocity structure is routinely invoked in models of the parsec-scale jets in order to explain the wide range of Lorentz factors required by different observations in those cases. If a beamed inverse-Compton model is viable at all for kiloparsec-scale jets, velocity structure must be present there as well (as concluded by Hardcastle 2006). Our data are dominated by objects at large angles to the line of sight, and so would naturally be expected to give estimates of the bulk Lorentz factor that are appropriate to the slow-moving component of the jet. However, the presence of this slow-moving component in observations of jets even at a small angle to the line of sight certainly adds to the complications of detailed inverse-Compton modelling of FR II sources; the radio emission from the jet is the only independent information available on the electron density present, but the assumption that all the radio-emitting material moves at a single bulk speed which can be estimated from the X-rays is no longer valid in the presence of jet velocity structure. Ideally measurements of jet prominences could be used to constrain models with jet velocity structure, but even if our data were good enough (and we have seen that our capability to distinguish between models is limited only to the most obvious cases) there is as yet no constraint on how the jet speed and emissivity might vary as a function of radius, and so effectively no model to test. High-resolution radio observations of jets in FRIIs with next-generation instruments such as e-MERLIN and the EVLA are required to give observational constraints on the surface brightness of FR II jets at a range of angles to the line of sight as a function of jet radius. It may then be possible to apply the techniques described here to constrain the properties of a more complex model of jet speeds.

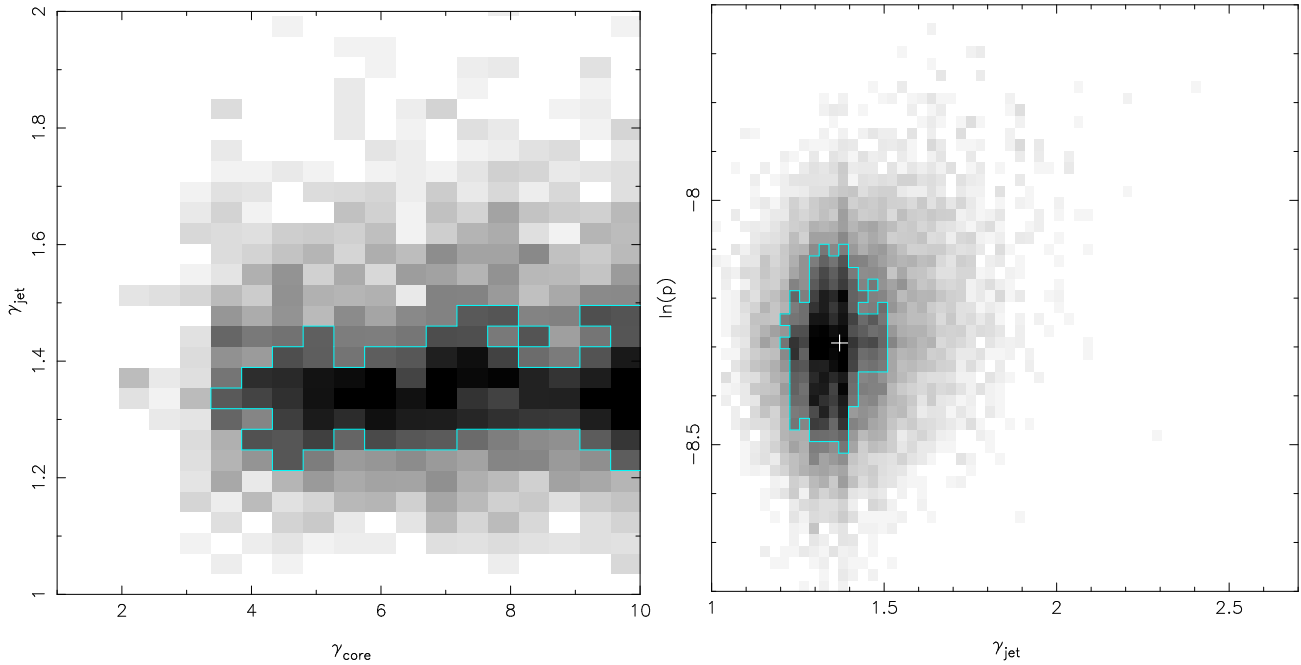


Figure 5. Posterior probability distribution for a joint fit to the jet and core prominence distributions with $\alpha = 0.5$. Left: the beaming parameters. Right: the jet beaming and prominence parameters for comparison with Fig. 3. The probability distributions are marginalized over all other parameters.

ACKNOWLEDGMENTS

We are very grateful to Mike Hobson for providing us with his METRO Markov-Chain Monte Carlo code with which the initial analysis for this project was carried out and which formed the basis of our own implementation of the technique. We also thank an anonymous referee for constructive comments on the first version of this paper. LMM thanks PPARC (now STFC) for a studentship and the astrophysics group at the Cavendish Laboratory, University of Cambridge, for support during the early stages of this work. MJH thanks the Royal Society for a research fellowship.

REFERENCES

- Arshakian, T. G., Longair, M. S., 2004, *MNRAS*, 351, 727
 Baars, J. W. M., Genzel, R., Pauliny-Toth, I. I. K., Witzel, A., 1977, *A&A*, 61, 99
 Barthel, P. D., 1989, *ApJ*, 336, 606
 Begelman, M. C., Fabian, A. C., Rees, M. J., 2008, *MNRAS*, 384, 19
 Black, A. R. S., Baum, S. A., Leahy, J. P., Perley, R. A., Riley, J. M., Scheuer, P. A. G., 1992, *MNRAS*, 256, 186
 Blandford, R. D., Rees, M. J., 1974, *MNRAS*, 169, 395
 Bridle, A. H., Perley, R. A., 1984, *ARA&A*, 22, 319
 Bridle, A. H., Hough, D. H., Lonsdale, C. J., Burns, J. O., Laing, R. A., 1994, *AJ*, 108, 766
 Celotti, A., Ghisellini, G., Chiaberge, M., 2001, *MNRAS*, 321, 1
 Chiaberge, M., Celotti, A., Capetti, A., Ghisellini, G., 2000, *A&A*, 358, 104
 Cohen, M. H., Lister, M. L., Homan, D. C., Kadler, M., Kellerman, K. I., Kovalev, Y. Y., Vermeulen, R. C., 2007, *ApJ*, 658, 232
 Fanaroff, B. L., Riley, J. M., 1974, *MNRAS*, 167, 31
 Garrington, S. T., Leahy, J. P., Conway, R. G., Laing, R. A., 1988
 Gilbert, G. M., Riley, J. M., Hardcastle, M. J., Croston, J. H., Pooley, G. G., Alexander, P., 2004, *MNRAS*, 351, 845
 Gregory, P. C., 2005, *Bayesian Logical Analysis for the Physical Sciences*, Cambridge University Press, Cambridge
 Hardcastle, M. J., 2006, *MNRAS*, 366, 1465
 Hardcastle, M. J., Alexander, P., Pooley, G. G., Riley, J. M., 1997, *MNRAS*, 288, 859
 Hardcastle, M. J., Alexander, P., Pooley, G. G., Riley, J. M., 1999, *MNRAS*, 304, 135 (H99)
 Hardcastle, M. J., Worrall, D. M., Birkinshaw, M., Canosa, C. M., 2003, *MNRAS*, 338, 176
 Hobson, M. P., Baldwin, J. E., 2004, *Appl. Opt.*, 43, 2651, 2004
 Hough, D. H., Vermeulen, R. C., Readhead, A. C. S., Cross, L. L., Barth, E. L., Yu, L. H., Beyer, P. J., Phifer, E. M., 2002, *AJ*, 123, 1258
 Jester, S., Meisenheimer, K., Martel, A. R., Perlman, E. S., Sparks, W. B., 2007, *MNRAS*, 380, 828
 Laing, R. A., *Nature*, 331, 149, 1988
 Laing, R. A., Riley, J. M., Longair, M. S., 1983, *MNRAS*, 204, 151 (LRL)
 Leahy, J. P., Black, A. R. S., Dennett-Thorpe, J., Hardcastle, M. J., Komissarov, S., Perley, R. A., Riley, J. M., Scheuer, P. A. G., 1997, *MNRAS*, 291, 20
 Lind, K. R., Blandford, R. D., 1985, *ApJ*, 295, 358
 Lister, M. L., Marscher, A. P., 1997, *ApJ*, 476, 572
 Liu, Y., Zhang, S. N., 2007, *ApJ*, 667, 724
 Mullin, L. M., Hardcastle, M. J., Riley, J. M., 2006, *MNRAS*, 372, 113
 Mullin, L. M., Riley, J. M., Hardcastle, M. J., 2008, *MNRAS*, 390, 595 (Paper I)
 Ryle, M. S., Longair, M. S., 1967, *MNRAS*, 136, 123
 Scheuer, P. A. G., 1974, *MNRAS*, 166, 513
 Scheuer, P. A. G., Readhead, A. C. S., 1979, *Nature*, 277, 182
 Schwartz, D. A., et al., 2000, *ApJ*, 540, L69
 Stawarz, L., Sikora, M., Ostrowski, M., Begelman, M. C., 2004, *ApJ*, 608, 95
 Tavecchio, F., Maraschi, L., Sambruna, R. M., Urry, C. M., 2000, *ApJ*, 544, 23
 Urry, C. M., Padovani, P., 1990, *ApJ*, 371, 60
 Urry, C. M., Shafer, R. A., 1984, *ApJ*, 280, 569
 Wardle, J. F. C., Aaron, S. B., 1997, *MNRAS*, 286, 425 (WA97)